Article

Enantiomer-dependent immunological response to chiral nanoparticles

https://doi.org/10.1038/s41586-021-04243-2

Received: 4 March 2020

Accepted: 15 November 2021

Published online: 19 January 2022

Check for updates

Liguang Xu[1,2,9], Xiuxiu Wang[1,2,9], Weiwei Wang[1,2], Maozhong Sun[1,2], Won Jin Choi[3], Ji-Young Kim[4], Changlong Hao[1,2], Si Li[5], Aihua Qu[1,2], Meiru Lu[1,2], Xiaoling Wu[1,2], Felippe M. Colombari[6], Weverson R. Gomes[7], Asdrubal L. Blanco[7], Andre F. de Moura[7], Xiao Guo[1,2], Hua Kuang[1,2,5,8]✉, Nicholas A. Kotov[3,4]✉ & Chuanlai Xu[1,2]✉

Chirality is a unifying structural metric of biological and abiological forms of matter. Over the past decade, considerable clarity has been achieved in understanding the chemistry and physics of chiral inorganic nanoparticles[1–4]; however, little is known about their effects on complex biochemical networks[5,6]. Intermolecular interactions of biological molecules and inorganic nanoparticles show some commonalities[7–9], but these structures differ in scale, in geometry and in the dynamics of chiral shapes, which can both impede and strengthen their mirror-asymmetric complexes. Here we show that achiral and left- and right-handed gold biomimetic nanoparticles show different in vitro and in vivo immune responses. We use irradiation with circularly polarized light (CPL) to synthesize nanoparticles with controllable nanometre-scale chirality and optical anisotropy factors (*g*-factors) of up to 0.4. We find that binding of nanoparticles to two proteins from the family of adhesion G-protein-coupled receptors (AGPCRs)—namely cluster-of-differentiation 97 (CD97) and epidermal-growth-factor-like-module receptor 1 (EMR1)—results in the opening of mechanosensitive potassium-efflux channels, the production of immune signalling complexes known as inflammasomes, and the maturation of mouse bone-marrow-derived dendritic cells. Both in vivo and in vitro immune responses depend monotonically on the *g*-factors of the nanoparticles, indicating that nanoscale chirality can be used to regulate the maturation of immune cells. Finally, left-handed nanoparticles show substantially higher (1,258-fold) efficiency compared with their right-handed counterparts as adjuvants for vaccination against the H9N2 influenza virus, opening a path to the use of nanoscale chirality in immunology.

Chiral inorganic nanostructures[1,3,4,10], obtained by a variety of methods[11–17], have been fuelling discoveries in optoelectronics, sensors and enantioselective catalysis, because of their strong chiroptical activity and ability to self-assemble. Racemic inorganic nanoparticles activate the immune system[18], and the nanoscale chirality of the particles may modulate their immunological properties because protein–protein complexes that govern immune responses also have nanoscale dimensions and mirror asymmetry[19]. Despite the commonality of chemical forces and possibility of forming lock-and-key complexes with proteins[7], the recognition of nanoparticle enantiomers by the immune system may be drastically impeded by the rigidity of the inorganic nanoparticle cores, because dynamic adaptation of the complex shapes of biomolecules is often required for lock-and-key interactions. Formation of protein coronas[20–22] may also 'camouflage' the asymmetry of particle core geometry. The study of immune-cell activation by nanoparticles with strong mirror asymmetry would shed light on the role of nanoscale chirality in systems-level biological responses, and inform methods for chirality-based design of nanoscale vaccine adjuvants.

Biomimetic nanoparticles display both molecular and nanoscale chirality[1], corresponding to the geometry of surface ligands and of the nanoparticles as a whole. Both scales of chirality can play a part in the activation of cell signalling networks, and one of the essential tasks of our work here is to differentiate their biological effects. However, because a typical synthesis of chiral nanoparticles involves coupled molecular and nanoscale chirality, it is difficult to unambiguously assign the biological effects to one or the other. To address this problem, we used a photosynthetic method for preparing gold nanoparticle enantiomers via illumination of seed particles with circularly polarized light (CPL) or linearly polarized light[23,24]. The degree of nanoparticle asymmetry can be varied by changing the parameters of illumination

[1]State Key Laboratory of Food Science and Technology, Jiangnan University, Wuxi, Jiangsu, China. [2]International Joint Research Laboratory for Biointerface and Biodetection, School of Food Science and Technology, Jiangnan University, Wuxi, Jiangsu, China. [3]Department of Materials Science and Engineering, University of Michigan, Ann Arbor, MI, USA. [4]Department of Chemical Engineering, Biointerface Institute, University of Michigan, Ann Arbor, MI, USA. [5]The Key Laboratory of Synthetic and Biological Colloids, Ministry of Education, School of Chemical and Material Engineering, Jiangnan University, Wuxi, Jiangsu, China. [6]Brazilian Nanotechnology National Laboratory, Brazilian Center for Research in Energy and Materials, Campinas, São Paulo, Brazil. [7]Department of Chemistry, Federal University of São Carlos, São Carlos, São Paulo, Brazil. [8]Science Center for Future Foods, Jiangnan University, Wuxi, Jiangsu, China. [9]These authors contributed equally: Liguang Xu, Xiuxiu Wang. ✉e-mail: kuangh@jiangnan.edu.cn; kotov@umich.edu; xcl@jiangnan.edu.cn

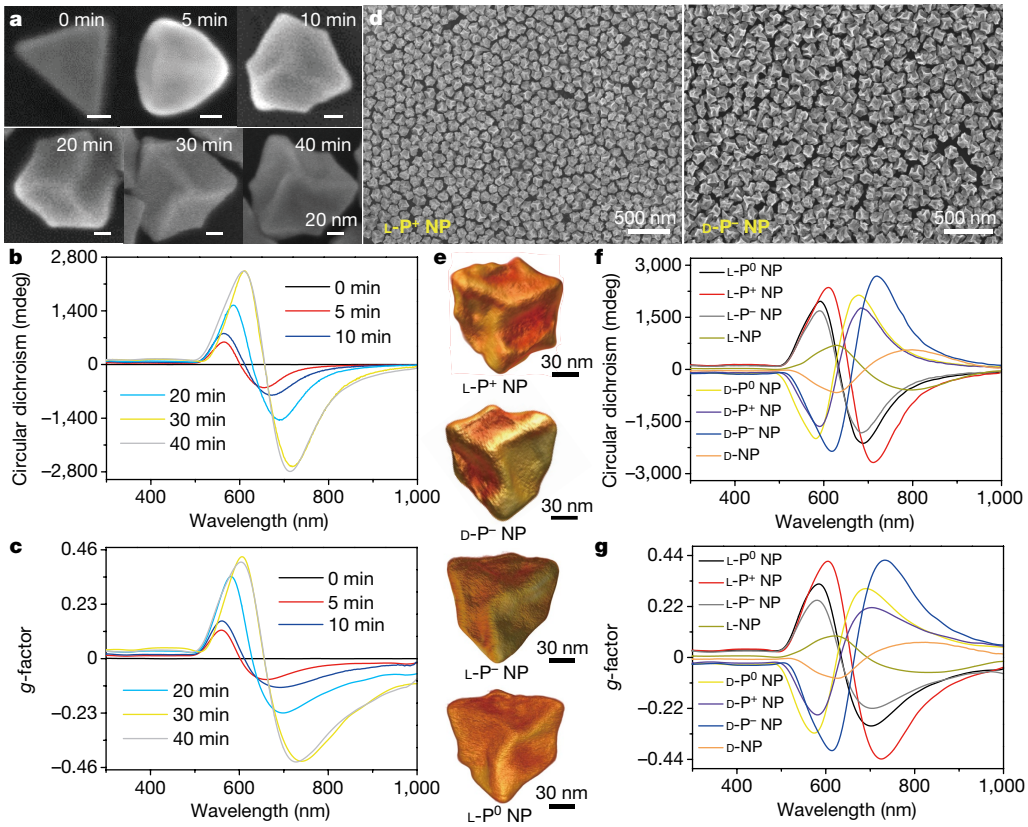

Fig. 1 | Morphology and spectroscopy of photosynthesized chiral nanoparticles (NPs). a–**c**, Scanning electron microscope (SEM) images (**a**), circular dichroism spectra (**b**) and *g*-factor spectra (**c**) of L-P$^+$ NPs after 0, 5, 10, 20, 30 and 40 min of illumination at 594 nm with 84 mW cm^{-2}. **d**, SEM images of L-P$^+$ NPs and D-P$^-$ NPs. **e**, TEM tomography images of L-P$^+$, D-P$^-$, L-P$^-$ and L-P^0 NPs. **f**, **g**, Circular dichroism spectra (**f**) and *g*-factor spectra (**g**) of NPs synthesized under different light conditions in the presence of CYP dipeptides: L-P$^+$ NPs (under LCP illumination), D-P$^-$ NPs (under RCP illumination), D-P$^+$ NPs (under LCP illumination), L-P$^-$ NPs (under RCP illumination), L-P^0 NPs (under LP illumination), D-P^0 NPs (under LP illumination), L-NPs (without light illumination) and D-NPs (without light illumination).

while keeping the chemical parameters constant. We used gold nanoprisms and other nanoparticles with achiral shapes (see Supplementary Information), stabilized by achiral ligands, as seeds[25]. The nanoparticles synthesized under CPL in the presence of different dipeptides are herein referred to as L/D-P^X nanoparticles. Here, L/D denotes the chirality of the L/D-dipeptide. X can be +, − or 0 and denotes the polarization of photons used in nanoparticle synthesis: + and − represent illumination conditions with, respectively, left circularly polarized light (LCP) and right circularly polarized light (RCP), leading to P$^+$ nanoparticles and P$^-$ nanoparticles, while 0 represents synthesis under linearly polarized light (Supplementary Table 1).

Multiparameter optimization of the photosynthetic protocols (Supplementary Figs. 1, 2) allowed us to produce large quantities of enantiopure clockwise or anticlockwise nanoparticles (Fig. 1a–c). The process involved left or right CPL illumination at 594 nm with an intensity of 84 mW cm^{-2} for 30 min in the presence of cysteine–phenylalanine (CYP) dipeptides. The resulting single-crystal gold nanoparticles displayed distinct chiral shapes and were roughly 120 nm in size (Fig. 1d and Supplementary Fig. 1); their size homogeneity (Supplementary Fig. 1) was improved compared with chiral nanoparticles synthesized by other means[11,26]. Evolution of morphology, chiroptical activities and hydrodynamic sizes of nanoparticles grown under different illumination conditions (Fig. 1a–c and Supplementary Fig. 2) indicate that the light-driven particle growth[24,27,28] was accompanied by chirality transfer from photons to nanoparticles, resulting in particles with high-index crystal planes[29].

The nanoparticles obtained after illumination retained some similarity to the original achiral nanoprisms, but acquired out-of-plane protrusions resembling propeller blades that led to strong geometrical and optical asymmetry (Fig. 2). L-P$^+$ nanoparticles and D-P$^-$ nanoparticles exhibited anticlockwise and clockwise rotation, respectively, of the three blades. Although the handedness of the nanoparticles is determined by their surface ligands, the maximum curvature of the blades, κ, is determined by the circular polarization of incident photons (Fig. 1e). For the same surface ligand, the magnitudes of the κ values for L-P$^+$ nanoparticles, L-P^0 nanoparticles and L-P$^-$ nanoparticles ($n = 5$, one type of chiral nanoparticle) were 0.029 ± 0.004, 0.023 ± 0.001 and 0.020 ± 0.002, respectively.

The nanoparticles with ligands of opposite chirality yielded nearly perfect mirror-symmetrical circular dichroism spectra. For example, the circular dichroism spectra of L-P$^+$ nanoparticles showed peaks at 605 (+) and 727 (−) nm, while those of D-P$^-$ nanoparticles displayed peaks in the same positions and with similar intensities, but the opposite signs (Fig. 1f, g). CPL resulted in considerably enhanced optical asymmetry *g*-factors that reached values as high as 0.42 at 605 (+) nm and 0.44 at 727 (−) nm for L-P$^+$ nanoparticles. These are the highest *g*-factors obtained for both singular nanoparticles and their assemblies to date[11–17,29]. L-P$^-$ and L-P^0 nanoparticles also exhibited high *g*-factors of 0.25 and 0.32 at roughly 600 (+) nm and 0.22 and 0.3 at roughly 700 (−) nm, respectively. The circular dichroism spectrum of D-P$^-$ nanoparticles was mirror-image symmetrical to that of L-P$^+$ nanoparticles, with peaks at 610 (−) and 732 (+) nm and equally high *g*-factors of 0.41 and 0.42, respectively. Note that the nanoparticles synthesized without illumination, that is, with L- or D-CYP dipeptides only, displayed maximum *g*-factors of 0.09 at 622 nm, which were 4.9-fold smaller than those of nanoparticles illuminated with CPL. Note also that the values of *g*-factors and κ (Fig. 1e–g) are interdependent, because the

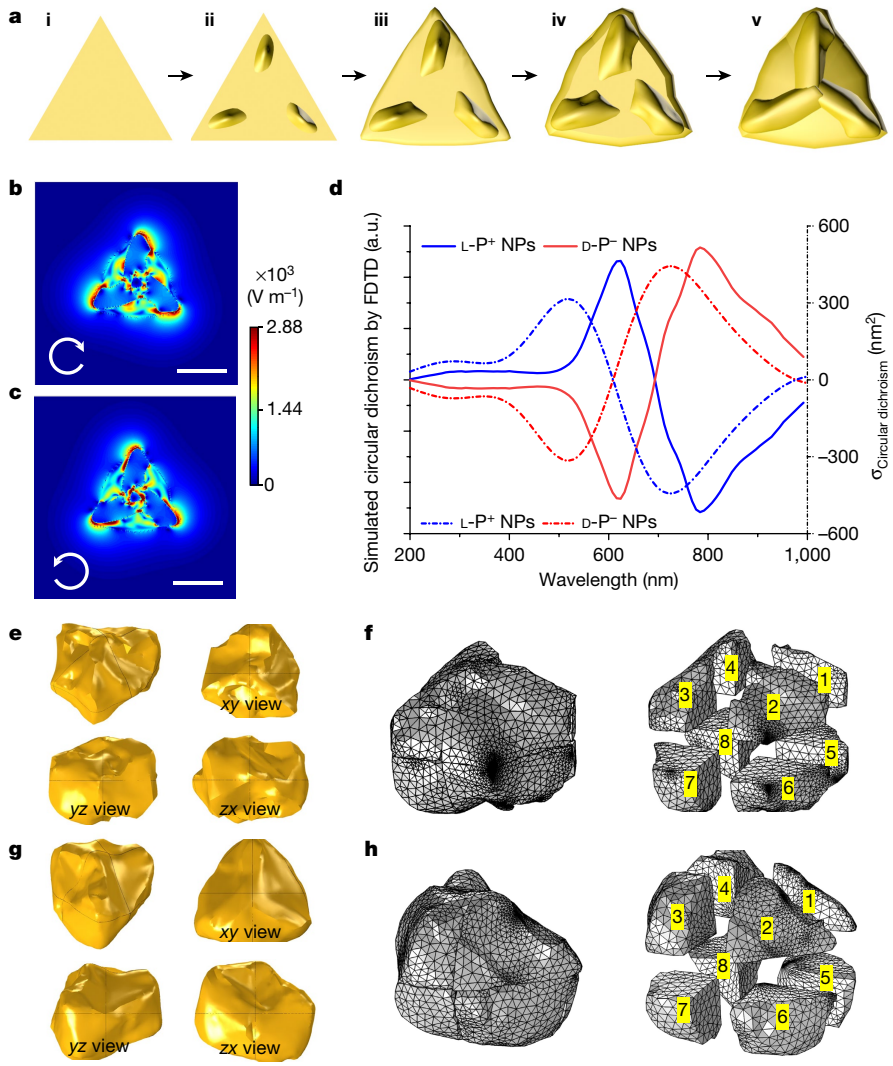

Fig. 2 | Quantification of electromagnetic fields and chirality measures for photosynthesized nanoparticles. a, Calculated stages (**i**–**v**) of gold deposition, based on the dynamic formation of hotspots on the surface of D-P⁻ NP trigonal nanoprisms under illumination with RCP. **b**, **c**, Electric field distribution of D-P⁻ NPs under LCP (**b**) and RCP (**c**) RCP. Scale bars, 50 nm. **d**, Solid lines (and left *y*-axis), circular dichroism spectra calculated from the model in **a** (stage **v**) using Lumerical software; dotted lines (and right *y*-axis), differences in extinction coefficients of L-P⁺ NP and D-P⁻ NP models (from Supplementary Fig. 3) obtained by electrodynamics calculations. **e**–**h**, Calculation of chirality measures based on the TEM tomography images of L-P⁺ NPs (**e**) and D-P⁻ NPs (**g**) from Fig. 1e, and division of L-P⁺ NPs (**f**) and D-P⁻ NPs (**h**) using the octants of the coordinate system following the methodology in ref. [23].

nanoscale dimensions of the blades result in strong asymmetric interaction with photons.

To identify the mechanisms underlying the CPL-mediated generation of chiral nanoparticles and their growth patterns, we carried out finite-difference time-domain (FDTD, Fig. 2a–c) and semi-empirical density functional theory (DFT, Supplementary Fig. 3) simulations of particle growth. The observed shapes of the nanoparticles can be explained by regioselective gold deposition on dynamically changing hotspots[28] and localized reduction of Au(III) to Au(0) (Supplementary Fig. 4). As the electrical field is strongly localized in the corners of the trigonal nanoprisms used as the seeds, the shape of the forming nanoparticles strongly depends on CPL (Fig. 2b, c and Supplementary Fig. 4). Using iterative modelling for progressive deposition of gold on gradually changing hotspots, we successfully modelled the final particle geometry with out-of-plane Au segments, which matched the key features of nanoparticle geometry observed by transmission electron microscopy (TEM) tomography (Fig. 1e). The simulated circular dichroism spectra for modelled nanoparticles are nearly identical to those obtained experimentally for L-P⁺ and D-P⁻ nanoparticles (Figs. 1f, 2d). We confirmed the growth mechanism for the synthesis of chiral nanoparticles induced by CPL, starting from gold nanocubes and octahedrons and using CYP and cysteine–proline (CPR) dipeptides as ligands, which also showed remarkably high chiroptical activity (Supplementary Fig. 5).

We calculated the Hausdorff chirality measure (HCM) and Osipov–Pickup–Dunmur (OPD) index as described[23] (Fig. 2e–h and Supplementary Table 2). HCM values for L-P⁺ nanoparticles and D-P⁻ nanoparticles are 0.0969 ± 0.0278 and 0.0774 ± 0.0187, respectively, showing similar quantitative degrees of chirality. Moreover, the signs of the OPD indexes are opposite for L-P⁺ nanoparticles and D-P⁻ nanoparticles, being 0.3420 ± 0.1014 and −0.2405 ± 0.0140, respectively. Both of these measures indicate that the synthesized nanoparticles are true geometrical enantiomers, which is important considering the parallels between the past studies of chirality in chemistry/biology and current studies of chirality in nanoparticles. Furthermore, it means that the amplitude of the circular dichroism and the maximal *g*-factors can be used as measures of the asymmetry of the nanoparticles, which are needed to assess the link between nanoscale chirality and the immune response.

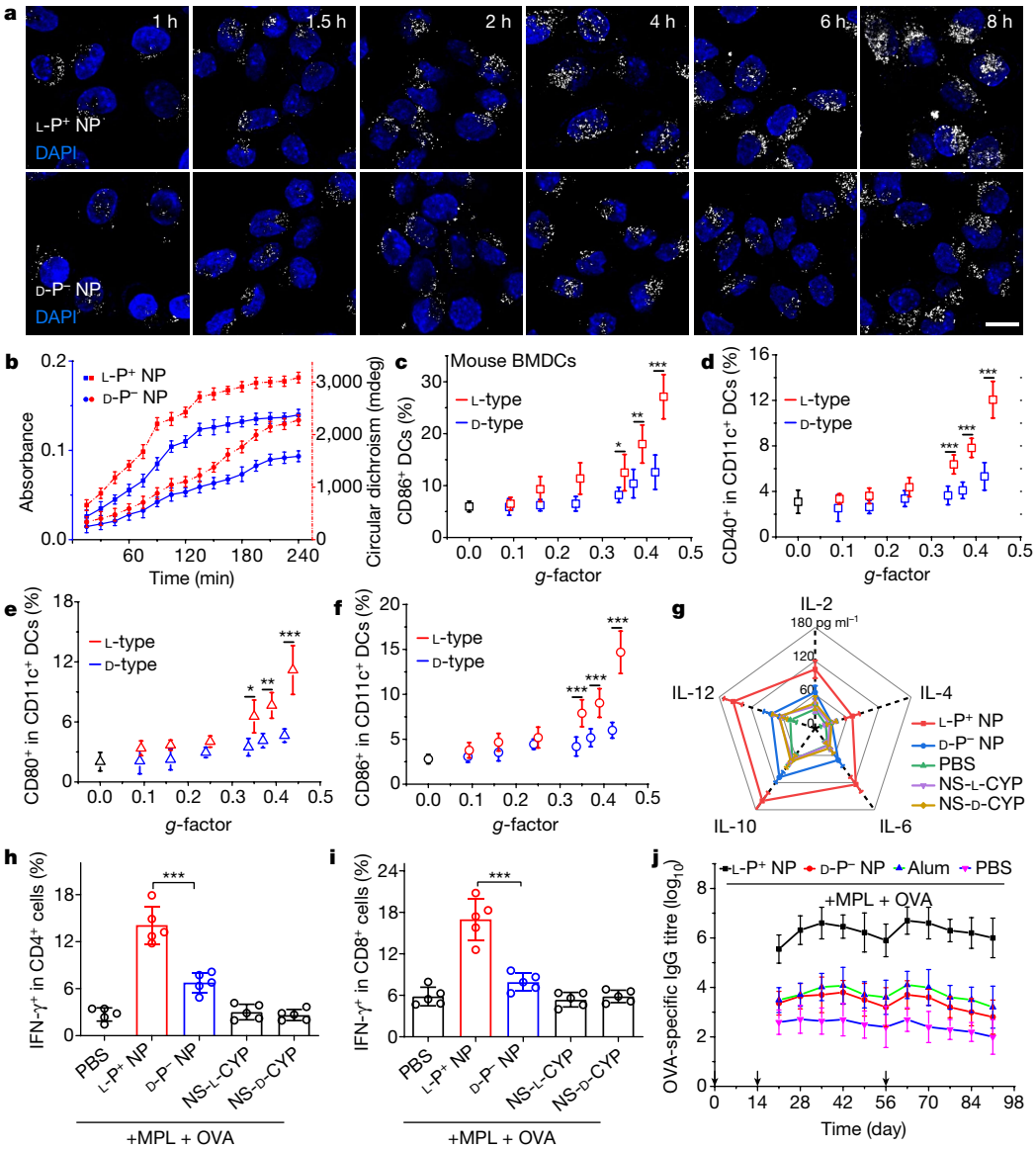

Fig. 3 | Nanoparticle-mediated immune responses. a, Two-photon luminescence (TPL) imaging of mouse BMDCs incubated with L-P$^+$ or D-P$^-$ NPs (2 nM) for up to 8 h. Cells were washed three times with Dulbecco's phosphate-buffered saline (PBS). Blue, DAPI (DNA stain); white, chiral NPs. Scale bars, 10 μm. **b**, Maximum absorption (blue) and the sum of absolute values for two circular dichroism extrema (red) varied with incubation time for mouse BMDCs incubated with L-P$^+$ NPs or D-P$^-$ NPs (2 nM) for 4 h. **c**, Mouse BMDCs were cultured with 2 μg ml^{-1} monophosphoryl lipid A (MPL), 20 μg ml^{-1} OVA and nanoprisms (*g*-factor 0), L-NPs (*g*-factor 0.09), D-NPs (*g*-factor 0.09), L-P^{+10} NPs (*g*-factor 0.16), D-P^{-10} NPs (*g*-factor 0.16), L-P^{+15} NPs (*g*-factor 0.25), D-P^{-15} NPs (*g*-factor 0.24), L-P^{+20} NPs (*g*-factor 0.35), D-P^{-20} NPs (*g*-factor 0.34), L-P^{+25} NPs (*g*-factor 0.39), D-P^{-25} NPs (*g*-factor 0.37), L-P$^+$ NPs (*g*-factor 0.44), and D-P$^-$ NPs (*g*-factor 0.42) for 12 h (2 nM), and CD86 levels were measured by flow cytometry (providing a measure of the percentage of dendritic cells, DCs). **d**–**f**, Expression of CD40 (**d**), CD80 (**e**) and CD86 (**f**) in recruited CD11c$^+$ DCs. C57BL/6 mice ($n = 5$) were subcutaneously immunized with different NPs (2 mg), MPL (10 μg), and OVA (50 μg). After 36 h, dLNs were collected, and expression of CD40, CD80 and CD86 was analysed by flow cytometry. **g**, Expression of IL-2, IL-4, IL-6, IL-10 and IL-12 in serum measured by ELISA 7 days after immunization. C57BL/6 mice ($n = 5$) were subcutaneously immunized with MPL (10 μg) plus OVA (50 μg), and phosophate-buffered saline (PBS), nanosphere (NS)-L-CYP, nanosphere (NS)-D-CYP, L-P$^+$ NPs and D-P$^-$ NPs (2 mg). **h**, **i**, IFN-γ$^+$ CD4$^+$ (**h**) and IFN-γ$^+$ CD8$^+$ (**i**) T cells in spleens measured by flow cytometry 7 days after immunization. **j**, Anti-OVA antibody titres in mouse serum. C57BL/6 mice ($n = 5$) were immunized with OVA and the indicated adjuvants (MPL, Alum + MPL, D-P$^-$ NP + MPL, L-P$^+$ NP + MPL) three times. Black arrows indicate immunization times. Data are means ± s.d. ($n = 5$). *$P < 0.05$, **$P < 0.01$, ***$P < 0.001$, analysed by Student's *t*-test.

The distinct nanoscale chirality, high colloidal stability and biological robustness of chiral gold nanoparticles (Fig. 1) made them suitable for evaluating in vivo and in vitro immune responses. We modified the particles with polyethylene glycol (PEG) to increase their stability and circulation time. Note that a PEG molecule is achiral and its coating is conformal; thus, it does not alter the chirality of the nanoparticles. We then incubated mouse bone-marrow-derived macrophages (BMMs) and mouse bone-marrow-derived dendritic cells (BMDCs) with the PEGylated L/D-P^X nanoparticles, finding high biocompatibility even after 12 h of incubation (Supplementary Fig. 6). We found that L-P$^+$ nanoparticles were taken up into BMDCs and BMMs with twofold greater efficiency than were D-P$^-$ nanoparticles, as determined by several independent experimental methods, namely two-photon luminescence (TPL) and circular dichroism and absorbance spectra (Fig. 3a, b and Supplementary Fig. 7). To eliminate the possibility that this difference in entry efficiency was associated with the chirality of the peptides, not of the nanoparticles, we removed the CYP stabilizers from the surface of the nanoparticles by incubation with dithiothreitol (DTT; Supplementary

Figs. 8, 9), and found that cellular uptake depended only on the chiral configuration of the nanoparticle itself. Following cellular uptake through the process of endocytosis, extracellular material is directed via intracellular pathways towards lysosomes; L-P$^+$ nanoparticles also showed a greater efficiency of escape from lysosomes than did D-P$^-$ nanoparticles (Supplementary Fig. 10). Biological TEM (bio-TEM) images showed the non-agglomerated states of nanoparticles at different stages of endocytosis (Supplementary Figs. 11, 12), indicating that the geometry of individual particles, rather than of particle aggregates, determines the uptake and lysosomal escape efficiency of nanoparticles. Electron microscopy data suggest that endocytosis of L-P$^+$ nanoparticles is faster than that of D-P$^-$ nanoparticles and involves stronger association with cellular membranes. The monotonic dependence of nanoparticle uptake by mouse BMDCs and mouse BMMs on the *g*-factor of the nanoparticles confirms the dependence of the endocytosis rate on the nanoscale chirality of the particles (Fig. 3 and Supplementary Figs. 13–16).

We further examined expression of the co-stimulatory biochemical markers CD40, CD80, CD86, SIINFEKL–MHC I and MHC II and of the pro-inflammatory cytokines interleukin (IL)-12 and tumour necrosis factor-α (TNF-α) by mouse BMDCs in response to nanoparticles, finding that L-P$^+$ nanoparticles induced greater expression than D-P$^-$ nanoparticles (Supplementary Fig. 14). Similarly, levels of IL-1β, IL-12 and TNF-α produced by mouse BMM cultures after incubation with L-P$^+$ nanoparticles were 1.9-fold ($P < 0.001$), 2.3-fold ($P < 0.001$) and 2.3-fold ($P < 0.001$) higher, respectively, than those produced by incubation with D-P$^-$ nanoparticles (Supplementary Fig. 15). We observed a distinct correlation between *g*-factors of nanoparticles and the immunological response of mouse BMDCs for both left- and right-handed enantiomers (namely L-P$^+$ nanoparticles and D-P$^-$ nanoparticles), whereas the levels of CD86 produced in response to achiral/racemic nanoprisms and nanoparticles were low (Fig. 3c). The amount of SIINFEKL–MHC I complexes found on mouse BMDCs was 2.1-fold higher ($P < 0.001$) after incubation with L-P$^+$ nanoparticles than with D-P$^-$ nanoparticles (Supplementary Fig. 14). Antigen uptake was not affected by any of the nanoparticle enantiomers (Supplementary Fig. 16).

Other benchmark findings include: first, the expression of CD86 remained unchanged after modification of nanoparticles with DTT (Supplementary Fig. 14); second, activation of immune cells by CYP alone was not observed; and third, immune responses to symmetric gold prisms, achiral nanoparticles coated with L/D-CYP (120 ± 6 nm) or nanospheres coated with L/D-CYP (30 ± 2 nm) were negligible, as were their circular dichroism amplitudes (Supplementary Figs. 14, 15). Thus, one can firmly conclude, first, that the biological response of immune cells to left- and right-handed nanoscale enantiomers is distinctly asymmetric; and, second, that this difference originates from a sequence of particle-specific biochemical signalling events related to their intracellular uptake.

To evaluate whether the asymmetry in the in vitro immune response is also seen at the organism level[9,18,30–32], we subcutaneously immunized C57BL/6 female mice with 2 mg of nanoparticles of different chiralities. Flow cytometry showed that the levels of CD40, CD80 and CD86 in the draining lymph nodes (dLNs) were markedly upregulated in CD11c$^+$ immune cells after stimulation with chiral nanoparticles for 36 h (Fig. 3d–f and Supplementary Fig. 17), which is consistent with the enhanced maturation of mouse BMDCs in vitro. The expression levels of CD40, CD80 and CD86 following treatment with L-P$^+$ nanoparticles (12.06 ± 1.61%, 11.19 ± 2.44% and 14.68 ± 2.36%) were 2.27-fold ($P < 0.001$), 2.42-fold ($P < 0.001$), and 2.45-fold ($P < 0.001$), respectively, higher than those produced by treatment with D-P$^-$ nanoparticles (5.32 ± 1.21%, 4.63 ± 0.66%, 6.00 ± 0.87%). As in the in vitro response, the expression levels of the cytokines increased as the *g*-factors of both types of nanoparticles increased. The achiral and racemic particles showed limited enhancement (Supplementary Figs. 15, 17), substantiating the relationship between nanoscale chirality and enhanced immune responses.

We also profiled cytokine release in the serum and spleens of mice seven days after immunization. Expression of IL-2, IL-4, IL-6, IL-10 and IL-12 was the greatest after injection of L-P$^+$ nanoparticles (Fig. 3g and Supplementary Fig. 17), indicating that the left-handed nanoparticles enhanced immune responses in mice. We found further evidence of this effect by evaluating the secretion of interferon (IFN)-γ and TNF-α: mice immunized with L-P$^+$ nanoparticles showed stronger secretions from CD4$^+$ T cells (2.08-fold and 1.98-fold for IFN-γ and TNF-α, respectively) and CD8$^+$ T cells (2.15-fold and 1.86-fold) than with D-P$^-$ nanoparticles (Fig. 3h, i and Supplementary Fig. 17). Moreover, the production of ovalbumin (OVA)-specific antibody was 1,584-fold higher after injection of L-P$^+$ nanoparticles than after D-P$^-$ nanoparticles (Fig. 3j and Supplementary Fig. 17). These data show that L-P$^+$ nanoparticles stimulate a stronger in vivo immune response than D-P$^-$ nanoparticles, complementing our in vitro findings. In addition, the subpopulations of central memory (CD44$^+$ and CD62L$^+$) and effector memory (CD44$^+$ and CD62L$^-$) T cells amongst CD4$^+$ and CD8$^+$ T cells were maintained after injection of L-P$^+$ nanoparticles (Supplementary Fig. 18). No obvious histological cytotoxicity was evident in the tissues examined from each group (Supplementary Fig. 19).

We next explored the biological mechanisms underlying the different immunological responses to left- and right-handed nanoparticle enantiomers in mouse BMDCs (Figs. 4a, b). The large AGPCR family of receptors attracted our attention because they have large flexible extracellular domains, which are easily accessible to nanoparticles[33,34]. Furthermore, these domains—and AGPCR receptors in general—are related to cell adhesion, signalling and endocytosis. These receptors are also commonly found in many immune cells. We first examined the interactions of EMR1, which is typical of mice, and then extended our study to CD97, which is common to murine and human immune cells. Both receptors have an extracellular chiral segment of up to five or six epidermal growth factor (EGF)-like domains, connected to a flexible chain[35–39]. The binding affinity, K_a, between L-P$^+$ nanoparticles and CD97 or EMR1 in cell-free buffer was, respectively, 14.0 ± 0.9-fold or 3.6 ± 1.2-fold higher than that for D-P$^-$ nanoparticles (Fig. 4c, d and Supplementary Fig. 20). The absolute K_a values for binding of L-P$^+$ nanoparticles to CD97 and EMR1 are $(1.8 \pm 0.2) \times 10^7\ M^{-1}$ and $(1.5 \pm 0.15) \times 10^4\ M^{-1}$, respectively, which is sufficient for assessment of K_a for cell signalling events[40]. These values are comparable to typical K_a values reported for receptors, being in the range $10^3\ M^{-1}$ to $10^9\ M^{-1}$ (ref. [41]).

In agreement with the data in Fig. 3c–f and Supplementary Figs. 21, 22, we found that the difference in immune response for left- and right-handed nanoparticle enantiomers increases as *g*-factors become larger. To test whether CD97 and EMR1 are involved in the uptake of nanoparticles by mouse immune cells (Fig. 4b), we blocked these receptors using antibodies. Endocytosis was reduced further when blocking CD97 rather than EMR1, because of the higher affinity of CD97 for nanoparticles. When both antibodies were used simultaneously, the cellular uptake of nanoparticles was almost completely inhibited, indicating that the biological activity of the nanoparticles is mediated by their interactions with CD97 and EMR1 (Fig. 4, Extended Data Fig. 1 and Supplementary Figs. 23, 24).

In terms of downstream immune signalling, confocal imaging showed expression of the NLR-family pyrin-domain-containing protein 3 (NLRP3) (a component of the inflammasome complex) and caspase-1 (activated by the inflammasome) (Extended Data Fig. 1c and Supplementary Figs. 25, 26) after incubation of mouse BMDCs with L-P$^+$ nanoparticles or D-P$^-$ nanoparticles for 12 h. When the inhibitor MCC950 was used to block NLRP3, the level of NLRP3 and caspase-1 dramatically decreased, indicating that the downstream inflammasome pathway is activated in BMDCs treated with chiral nanoparticles. Notably, L-P$^+$ nanoparticles led to stronger inflammasome activation than D-P$^-$ nanoparticles. The amount of IL-1β secreted was also increased to a greater degree in response to L-P$^+$ nanoparticles than D-P$^-$ nanoparticles (Extended Data Fig. 2a and Supplementary Fig. 25).

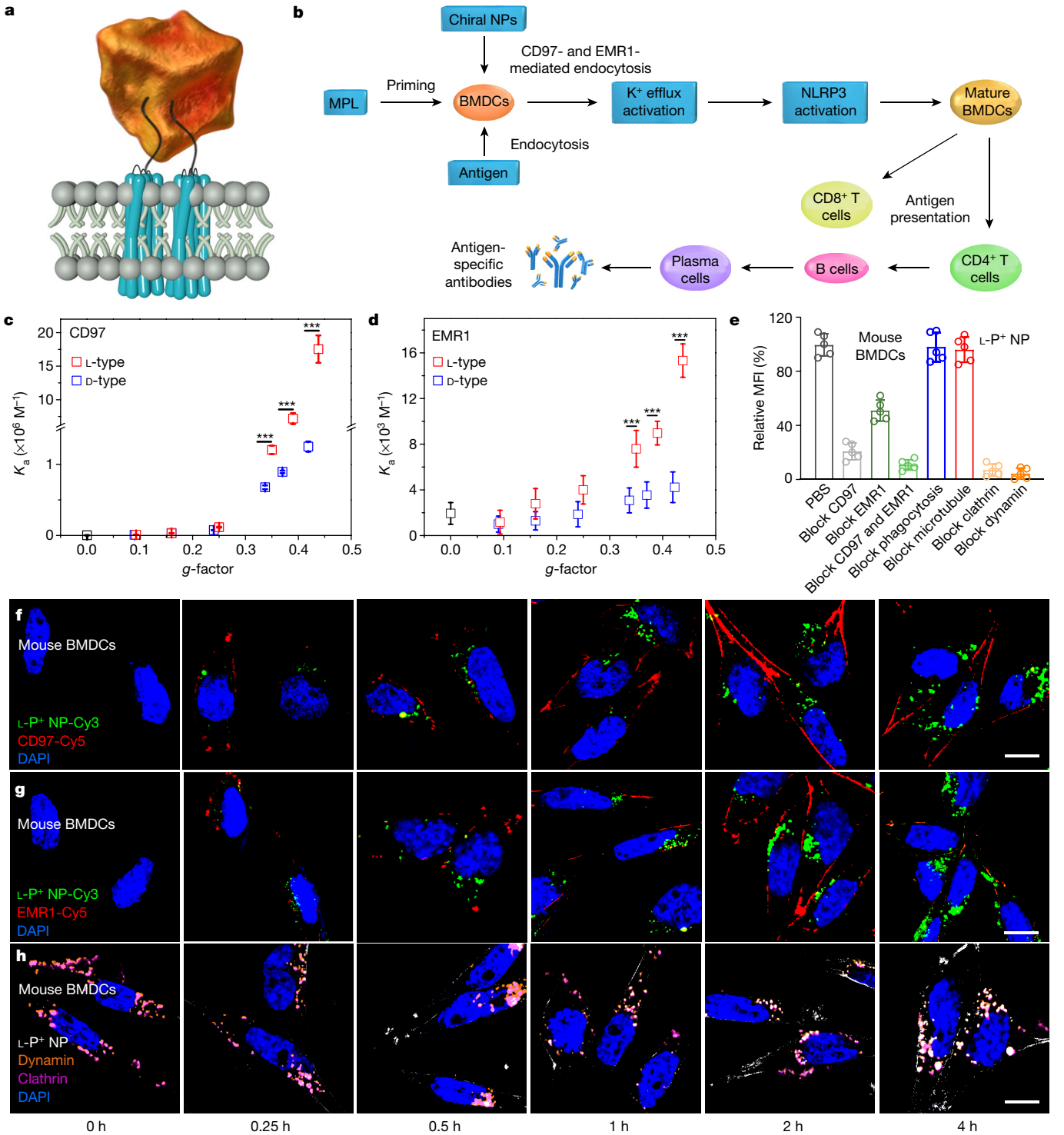

Fig. 4 | Chirality-dependent intracellular intake of BMDCs. a, Diagram showing the interaction of chiral NPs with extracellular chiral chains of EGF-like domains on cellular AGPCR receptors. **b**, The mechanism of induction of immune responses by chiral NPs. **c**, **d**, Binding affinity, K_a, between CD97 and different chiral NPs (**c**) and between EMR1 and different chiral NPs (**d**) in cell-free buffer. For CD97, the K_a for the left enantiomer was $1.8 \pm 0.2 \times 10^7\ M^{-1}$ and for the right enantiomer was $1.3 \pm 0.1 \times 10^6\ M^{-1}$; for EMR1, the K_a for the left enantiomer was $1.5 \pm 0.15 \times 10^4\ M^{-1}$ and for the right enantiomer was $4.2 \pm 1.3 \times 10^3\ M^{-1}$. **e**, Flow-cytometry data for mouse BMDCs after being treated with PBS, anti-EMR1 antibody (5 μg ml^{-1}, 'Block EMR1'), anti-CD97 antibody (10 μg ml^{-1}), anti-EMR1 (5 μg ml^{-1}) plus anti-CD97 (10 μg ml^{-1}) antibodies, cytochalasin D (phagocytosis inhibitor), nocodazole (microtubule inhibitor), chlorpromazine (clathrin inhibitor) or dynasore (dynamin inhibitor). Cells were subsequently incubated with L-P$^+$ NPs (2 nM). **f**, **g**, Confocal imaging of mouse BMDCs incubated with 2 μg ml^{-1} MPL, 20 μg ml^{-1} OVA and 2 nM L-P$^+$ NPs for various incubation times (up to 4 h). Blue, DAPI; red, CD97–Cy5 (f) or EMR1–Cy5 (**g**); green: L-P$^+$ NP–Cy3. Scale bar, 10 μm. **h**, TPL imaging of mouse BMDCs incubated with 2 nM L-P$^+$ NPs with various incubation times (up to 4 h). Blue, DAPI; orange, dynamin; pink, clathrin; white: L-P$^+$ NPs. Scale bar, 10 μm. Data are means ± s.d. ($n = 5$). $^*P < 0.05$, $^{**}P < 0.01$, $^{***}P < 0.001$, analysed by Student's *t*-test.

We confirmed the large difference in immune response for the two nanoparticle enantiomers by western blot and reverse transcription with polymerase chain reaction (RT–PCR) (Supplementary Figs. 25, 26). These methods corroborated the microscopy data, showing that expression of NLRP3, IL-1β and caspase-1 in BMDCs is considerably higher in response to L-P^+ nanoparticles than D-P^- nanoparticles. Again, the degree of inflammasome activation for nanoparticles of the same handedness increased as the *g*-factor increased (Extended Data Fig. 2b). In a negative benchmark experiment, inflammasomes from BMDCs of NLRP3-knockout mice could not be activated by chiral nanoparticles (Supplementary Fig. 25).

Looking further into the downstream processes of the immune response, in vivo experiments showed that the nanoparticles triggered activation of NLRP3 inflammasomes in the lymph nodes of C57BL/6 mice 36 h after subcutaneous injection (Extended Data Fig. 2b and Supplementary Fig. 27). Expression of CD40, CD80, CD86, SIINFEKL–MHC I and MHC II (Supplementary Fig. 17) was also markedly elevated after nanoparticle injection. By contrast, expression of the same biochemical markers and OVA-specific antibody titres in NLRP3-knockout mice was weak after the same nanoparticle injections (Supplementary Fig. 27). These data firmly establish that chiral nanoparticles enhance the immune response by activating the NLRP3 inflammasome pathway.

To explore exactly how chiral nanoparticles induce the inflammasome response, we investigated inflammasome activity after blocking different signalling pathways. The activity of NLRP3 inflammasomes induced by chiral nanoparticles in mouse BMDCs was not affected by cytochalasin D (an inhibitor of phagocytosis), *N*-acetyl-L-cysteine (an inhibitor of reactive oxygen species), nocodazole (a microtubule inhibitor) or CA-074-Me (an inhibitor of cathepsin B) (Extended Data Fig. 1c and Supplementary Fig. 25). Only when the K^+ ion channel was blocked by amiodarone was the expression of inflammasomes substantially attenuated. Incubation of BMDCs with 130 mM KCl, which completely inhibits K^+ efflux, also showed the central role of the K^+ channel in nanoparticle-mediated activation of the inflammasome pathway. Further support for this mechanism is provided by literature data on K^+-efflux-mediated inflammasome activation[42], and by our enzyme-linked immunosorbent assay (ELISA), western blot and RT–PCR data (Supplementary Fig. 25).

Discussion

The different stages in the immune response to L-P^+ or D-P^- nanoparticles are shown in Fig. 4b. First, both types of chiral nanoparticle undergo endocytosis mediated by CD97 and EMR1 (ref. [34]). However, the left-handed enantiomers associate with these AGPCR-family receptors more strongly than do the right-handed ones. L-P^+ nanoparticles are likely to have higher binding affinity than D-P^- nanoparticles for CD97 and EMR1, owing to supramolecular interactions between the chiral extracellular domains made (in both receptors) from EGF-like segments and the curved chiral nanoparticles. Nanoparticles may also cause differential clustering of the AGPCR receptors in the membrane. Second, mechanical stress applied to the cellular membrane by the nanoparticles results in signalling of mechanosensitive K^+ efflux channels[18,42–45] to the NLRP3 inflammasome pathway. Third, the stronger binding of L-P^+ nanoparticles to the receptors leads to greater inflammasome production, which triggers the stronger immune responses to L- than D-enantiomers.

To investigate the significance of nanoscale chirality in systems-level biological responses and the potential of L-P^+ and D-P^- nanoparticles as vaccine adjuvants, we injected C57BL/6 mice with H9N2 influenza vaccine mixed with different nanoparticles (Extended Data Fig. 2 and Supplementary Fig. 28). In agreement with our in vitro and in vivo data above, left-handed nanoparticles produced a greater increase in the influenza-specific antibody titre than their right-handed counterparts: after injection of L-P^+ nanoparticles, the response was 1,258-fold higher than after D-P^- nanoparticles, and lasted for as long as 91 days.

The proliferation of IFN-γ secreting $CD4^+$ T cells (15.68 ± 1.66%), IFN-γ secreting $CD8^+$ T cells (17.80 ± 2.88%) and IL-4 secreting $CD4^+$ T-cells (12.52 ± 1.92%) in mouse spleen was 1.85, 1.81 and 2.11-fold higher, respectively, after activation by L-P^+ nanoparticles compared with D-P^- nanoparticles (Extended Data Fig. 2d–f). Hyperaemia and hyperplasia with infiltration of inflammatory cells were observed in mice treated with D-P^- nanoparticles 21 days after being challenged with H9N2 influenza (Supplementary Fig. 28). Severe pulmonary haemorrhages and lung abscesses were observed in response to commercial alum adjuvant or achiral nanoparticles, but there were no discernible histopathological lesions found in mice that received *L*-P^+ nanoparticles. Therefore, L-P^+ nanoparticles bolster the immune response to a greater degree than do D-P^- nanoparticles. The adjuvant performance of chiral nanoparticles was not reduced after coating with DTT, showing the importance of the chirality of the nanoparticle as a whole for enhancing in vivo immune responses. These findings were verified by the negligible activation of the immune system in multiple control groups (Extended Data Fig. 2c–f).

In conclusion, in vitro and in vivo immune responses to nanoparticle enantiomers and their achiral homologue differ substantially, which is due to chirality-dependent differences in endocytosis into immune cells. These findings demonstrate the need for the parametrization of nanoparticle chirality in biomedical and toxicological studies using g-factor, OPD or HCM. The described chiral effects also raise the possibility of tailoring immune responses using precisely engineered chiral inorganic nanostructures, leading to a better understanding of their role in biological systems.

Online content

Any methods, additional references, Nature Research reporting summaries, source data, extended data, supplementary information, acknowledgements, peer review information; details of author contributions and competing interests; and statements of data and code availability are available at https://doi.org/10.1038/s41586-021-04243-2.

1. Ma, W. et al. Chiral inorganic nanostructures. *Chem. Rev.* **117**, 8041–8093 (2017).
2. Copeland, L. O. & McDonald, M. B. in *Principles of Seed Science and Technology* 59–110 (Springer, 1999).
3. Zhang, Q. et al. Unraveling the origin of chirality from plasmonic nanoparticle-protein complexes. *Science* **365**, 1475–1478 (2019).
4. Guerrero-Martínez, A., Alonso-Gómez, J. L., Auguié, B., Cid, M. M. & Liz-Marzán, L. M. From individual to collective chirality in metal nanoparticles. *Nano Today* **6**, 381–400 (2011).
5. Kuznetsova, V. A. et al. Enantioselective cytotoxicity of ZnS:Mn quantum dots in A549 cells. *Chirality* **29**, 403–408 (2017).
6. Sun, M. et al. Site-selective photoinduced cleavage and profiling of DNA by chiral semiconductor nanoparticles. *Nat. Chem.* **10**, 821–830 (2018).
7. Kotov, N. A. Inorganic nanoparticles as protein mimics. *Science* **330**, 188–189 (2010).
8. Cagno, V. et al. Broad-spectrum non-toxic antiviral nanoparticles with a virucidal inhibition mechanism. *Nat. Mater.* **17**, 195–203 (2018).
9. Wang, D. et al. Engineering nanoparticles to locally activate T cells in the tumor microenvironment. *Sci. Immunol.* **4**, eaau6584 (2019).
10. Gérard, V. A. et al. Plasmon-induced CD response of oligonucleotide-conjugated metal nanoparticles. *Chem. Commun.* **47**, 7383 (2011).
11. Yeom, J. et al. Chiromagnetic nanoparticles and gels. *Science* **359**, 309–314 (2018).
12. Ma, W. et al. Attomolar DNA detection with chiral nanorod assemblies. *Nat. Commun.* **4**, 2689 (2013).
13. Zheng, G. et al. Tuning the morphology and chiroptical properties of discrete gold nanorods with amino acids. *Angew. Chem. Int. Edn* **57**, 16452–16457 (2018).
14. Chen, W. et al. Nanoparticle Superstructures Made by Polymerase Chain Reaction: Collective Interactions of Nanoparticles and a New Principle for Chiral Materials. *Nano Lett.*, **9**, 2153–2159 (2009).
15. Singh, G. et al. Self-assembly of magnetite nanocubes into helical superstructures. *Science* **345**, 1149–1153 (2014).
16. Molotsky, T., Tamarin, T., Ben Moshe, A., Markovich, G. & Kotlyar, A. B. Synthesis of chiral silver clusters on a DNA template. *J. Phys. Chem. C* **114**, 15951–15954 (2010).
17. Im, S. W. et al. Chiral surface and geometry of metal nanocrystals. *Adv. Mater.* **32**, 1905758 (2020).
18. Wang, J. et al. Physical activation of innate immunity by spiky particles. *Nat. Nanotechnol.* **13**, 1078–1086 (2018).
19. Geva, M., Frolow, F., Eisenstein, M. & Addadi, L. Antibody recognition of chiral surfaces. Enantiomorphous crystals of leucine-leucine-tyrosine. *J. Am. Chem. Soc.* **125**, 696–704 (2003).

20. Walkey, C. D., Olsen, J. B., Guo, H., Emili, A. & Chan, W. C. W. Nanoparticle size and surface chemistry determine serum protein adsorption and macrophage uptake. *J. Am. Chem. Soc.* **134**, 2139–2147 (2012).
21. del Pino, P. et al. Protein corona formation around nanoparticles—from the past to the future. *Mater. Horiz.* **1**, 301–313 (2014).
22. Wang, X. et al. Chiral surface of nanoparticles determines the orientation of adsorbed transferrin and its interaction with receptors. *ACS Nano* **11**, 4606–4616 (2017).
23. Kim, J.-Y. et al. Assembly of gold nanoparticles into chiral superstructures driven by circularly polarized light. *J. Am. Chem. Soc.* **141**, 11739–11744 (2019).
24. Yeom, J. et al. Chiral templating of self-assembling nanostructures by circularly polarized light. *Nat. Mater.* **14**, 66–72 (2015).
25. Ou, Z., Wang, Z., Luo, B., Luijten, E. & Chen, Q. Kinetic pathways of crystallization at the nanoscale. *Nat. Mater.* **19**, 450–455 (2020).
26. Karst, J. et al. Chiral scatterometry on chemically synthesized single plasmonic nanoparticles. *ACS Nano* **13**, 8659–8668 (2019).
27. González-Rubio, G. et al. Femtosecond laser reshaping yields gold nanorods with ultranarrow surface plasmon resonances. *Science* **358**, 640–644 (2017).
28. Saito, K. & Tatsuma, T. Chiral plasmonic nanostructures fabricated by circularly polarized light. *Nano Lett.* **18**, 3209–3212 (2018).
29. Lee, H.-E. et al. Amino-acid- and peptide-directed synthesis of chiral plasmonic gold nanoparticles. *Nature* **556**, 360–365 (2018).
30. Zhang, Q. et al. Neutrophil membrane-coated nanoparticles inhibit synovial inflammation and alleviate joint damage in inflammatory arthritis. *Nat. Nanotechnol.* **13**, 1182–1190 (2018).
31. Pelliccia, M. et al. Additives for vaccine storage to improve thermal stability of adenoviruses from hours to months. *Nat. Commun.* **7**, 13520 (2016).
32. Xia, Y. et al. Exploiting the pliability and lateral mobility of Pickering emulsion for enhanced vaccination. *Nat. Mater.* **17**, 187–194 (2018).
33. Langenhan, T., Aust, G. & Hamann, J. Sticky signaling—adhesion class G protein-coupled receptors take the stage. *Sci. Signal.* **6**, re3 (2013).
34. Oldham, W. M. & Hamm, H. E. Heterotrimeric G protein activation by G-protein-coupled receptors. *Nat. Rev. Mol. Cell Biol.* **9**, 60–71 (2008).
35. Ferguson, S. M. & De Camilli, P. Dynamin, a membrane-remodelling GTPase. *Nat. Rev. Mol. Cell Biol.* **13**, 75–88 (2012).
36. Richards, D. M. & Endres, R. G. Target shape dependence in a simple model of receptor-mediated endocytosis and phagocytosis. *Proc. Natl Acad. Sci. USA* **113**, 6113–6118 (2016).
37. Mahmoudi, M., Azadmanesh, K., Shokrgozar, M. A., Journeay, W. S. & Laurent, S. Effect of nanoparticles on the cell life cycle. *Chem. Rev.* **111**, 3407–3432 (2011).
38. Murray, P. J. & Wynn, T. A. Protective and pathogenic functions of macrophage subsets. *Nat. Rev. Immunol.* **11**, 723–737 (2011).
39. Ohta, S., Glancy, D. & Chan, W. C. W. DNA-controlled dynamic colloidal nanoparticle systems for mediating cellular interaction. *Science* **351**, 841–845 (2016).
40. Naur, P. et al. Ionotropic glutamate-like receptor 2 binds D-serine and glycine. *Proc. Natl Acad. Sci. USA* **104**, 14116–14121 (2007).
41. Cobb, M. H. & Ross, E. M. in *Mol. Biol. Cell* 6th edn (eds Alberts, B. et al.) 589–643 (Garland, 2002).
42. Muñoz-Planillo, R. et al. K^+ efflux is the common trigger of NLRP3 inflammasome activation by bacterial toxins and particulate matter. *Immunity* **38**, 1142–1153 (2013).
43. Kefauver, J. M., Ward, A. B. & Patapoutian, A. Discoveries in structure and physiology of mechanically activated ion channels. *Nature* **587**, 567–576 (2020).
44. Ranade, S. S., Syeda, R. & Patapoutian, A. Mechanically activated ion channels. *Neuron* **87**, 1162–1179 (2015).
45. Galic, M. et al. External push and internal pull forces recruit curvature-sensing N-BAR domain proteins to the plasma membrane. *Nat. Cell Biol.* **14**, 874–881 (2012).

Methods

Synthesis of gold nanoprisms

In a typical synthetic process[46], 1.6 ml of 0.1 M cetrimonium chloride (CTAC) was injected into 8 ml of deionized water, followed by addition of 75 µl of 10 mM KI and 100.4 µl of sodium tetrachloroaurate solution (obtained by mixing $HAuCl_4$ and NaOH in a 1:1 ratio). Then, 80 µl of 64 mM ascorbic acid was quickly injected to reduce Au^{3+}; simultaneously, the colour of the solution changed from light yellowish to colourless. Finally, 10 µl of 0.1 M NaOH was rapidly injected into the solution to initiate the reduction of Au^{+} for 10 min. As the reaction was completed, the colour of the solution changed from colourless to blue.

Light-mediated synthesis of chiral nucleoproteins

The laser wavelength used in the illumination experiment lay within the ultraviolet–visible (UV–Vis) absorption range of the seeds and the circular dichroism of the chiral nanoparticle growth. For the chiral nanoparticles synthesized from the nanoprisms and octahedrons as seeds, we chose 594 nm of polarized light owing to the absorption spectra of the seeds. For chiral nanoparticles synthesized from nanocubes as seeds, we chose 532 nm polarized light. When the reaction was complete, the reaction solution was centrifuged twice (1,600*g*, 1 min) and resuspended in 1 mM CTAB or 5 mM CTAC.

To synthesize L/D-P^X nanoparticles, a growth solution was formed by adding 0.8 ml of 10 mM CTAB to 3.95 ml deionized water, followed by the addition of 0.2 ml of 10 mM $HAuCl_4$. After incubation for 5–10 min, 0.475 ml of 40 mM ascorbic acid was injected rapidly into the growth solution. Then, 5 µl of 4 mM L/D-CYP and 50 µl of seeds were injected into the growth solution, which was mixed thoroughly. Then, the reaction solution was injected into a quartz cuvette and immediately illuminated with various forms of polarized light (right circularly polarized light, RCP; linear polarized light, LP; left circularly polarized light, LCP) for 30 min. To obtain chiral nanoparticles with the best enhancement of chiroptical activity, we used a light wavelength of 594 nm and an intensity of 84 mW cm^{-2}.

To synthesize L/D-P^X NP-C, we created a growth solution by adding 1 ml of 0.15 M CTAC and 0.2 ml of 10 mM $HAuCl_4$ to 3.9 ml deionized water. After incubation for 5–10 min, 0.475 ml of 0.1 M ascorbic acid was injected rapidly into the growth solution. Then, 5 µl of 1 mM L/D-CYP and 50 µl of cube seeds were injected into the growth solution and mixed thoroughly. The reaction solution was injected into a quartz cuvette and immediately illuminated under different forms of polarized light (RCP, LP, LCP) for 30 min. In order to obtain chiral nanoparticles with the best enhancement in chiroptical activity, we set the wavelength of light to 532 nm and the light intensity to 84 mW cm^{-2}.

To synthesize L/D-P^X NP-O, we created a growth solution by adding 1 ml of 0.18 M CTAC and 0.2 ml of 10 mM $HAuCl_4$ to 3.9 ml deionized water. After incubation for 5–10 min, 0.475 ml of 0.3 M ascorbic acid was injected rapidly into the growth solution. Then, 5 µl of 1.2 mM L/D-CPR and 50 µl of octahedron seeds were injected into the growth solution and mixed thoroughly. The reaction solution was injected into a quartz cuvette and immediately illuminated under different forms of polarized light for 30 min. To obtain chiral nanoparticles with the best enhancement in chiroptical activity, we set the light wavelength to 594 nm and intensity to 84 mW cm^{-2}.

Calculation of anisotropy factor (*g*-factor) values

We calculated *g*-factors using the following formula:

$$g\text{-factor} = \text{circular dichroism (in mdeg)} / (32,980 \times \text{absorbance value})$$

where the circular dichroism values were acquired from circular dichroism spectra, and the light absorbance values were obtained from UV–Vis spectra.

PEGylated chiral nanoparticles

We added 100 µl mPEG-SH (molecular weight = 2,000; 50 mM) to 1 ml L-nanoparticles, L-P^{+10} nanoparticles, L-P^{+15} nanoparticles, L-P^{+20} nanoparticles, L-P^{+25} nanoparticles, L-P^{+} nanoparticles, prism, D-nanoparticles, D-P^{-10} nanoparticles, D-P^{-15} nanoparticles, D-P^{-20} nanoparticles, D-P^{-25} nanoparticles, D-P^{-} nanoparticles, nanoparticles, NP-D-CYP, NP-L-CYP, NS-L-CYP, NS-D-CYP, L-P^{+} nanoparticles plus DTT, and D-P^{-} nanoparticles plus DTT. After 12 h, the supernatant was discarded by centrifugation (1,700*g*, 1 min) and the sediment was resuspended in culture medium for in vitro and in vivo experiments.

FDTD simulations

Optical properties and growth mechanisms for Au chiral particles were simulated using FDTD software (Lumerical FDTD Solutions). The Au chiral nanoparticles were illuminated using a normally incident RCP or LCP plane wave propagating in the *z*-direction. We used the 'two sources in one simulation method' for making CPL. The phase of the source for the *x*-polarized plane wave was set to 0, and the phase of the source for the *y*-polarized plane wave was set to +90° or −90°. Positive and negative 90° of phase were defined as LCP and RCP, representing counterclockwise rotation and clockwise rotation along the propagation axis, respectively. The optical properties of gold were from ref. [47]. The chiral structure was excited by a source with a wavelength range of 200–1,000 nm, propagating along the negative *z*-direction. A simulation box of size 0.5 µm × 0.5 µm × 1.2 µm was used. Perfectly matched layer (PML) absorbing boundaries were applied for the top and bottom *x*–*y* planes, and periodic boundaries were applied for the front and back *x*–*z* planes and the left and right *y*–*z* planes. The geometries of chiral gold nanoparticles were reconstructed using numerical computing software (Matlab) and three-dimensional graphic software packages (3D Max 2017, Autodesk). Circular dichroism in the simulations was defined as $CD = |A_L - A_R|$, where A_L and A_R represent the absorbance of LCP and RCP photons, respectively.

Cells and cultures

Mouse BMMs were separated from C57BL/6 mice and cultured in PRMI 1640 medium plus 10% fetal bovine serum (FBS) with 100 ng ml^{-1} of macrophage colony-stimulating factor (Biolegend) for 7 days. Mouse BMDCs were separated from wild-type or NLRP3-knockout ($NLRP3^{-/-}$) C57BL/6 mice and cultured in PRMI 1640 medium plus 10% FBS with 10 ng ml^{-1} of granulocyte macrophage colony-stimulating factor (Biolegend) for 7 days. Human BMDCs, obtained from Procell Life Science &Technology, were cultured in PRMI 1640 medium plus 10% FBS for 7 days.

Apoptosis assays

Mouse BMMs and BMDCs or human BMDCs were seeded into 6-well plates at an initial density of 10^6 cells per well, and incubated with different concentrations of chiral nanostructures (0, 0.5, 1, 2 or 4 nM). After 12 h, the cells were harvested and stained with Annexin V and propidium iodide (PI) (Beyotime, C1052) for 15 min in the dark. Results were analysed with CytExpert.

Toxicity in vivo

All animal experiments complied with institutional ethical guidelines and the Committee on Animal Welfare of Jiangnan University.

The tail veins of C57BL/6 mice (female, 5–6 weeks) were injected with L-P^{+} nanoparticles and D-P^{-} nanoparticles (2 mg). On days 1, 3, 5, 7 or 15, the mice were euthanized, and the liver and kidney were excised for haematoxylin-and-eosin staining. Blood samples were collected on days 1, 3, 5, 7 and 15 by eyeball extraction and used to test liver and kidney function.

In vitro cellular uptake

Immune cells were seeded into six-well plates. The cells (1×10^6 cells per well) were incubated with nanomaterials (L-P^{+} nanoparticles,

D-P$^-$ nanoparticles, L-P$^+$ nanoparticles plus DTT, and D-P$^-$ nanoparticles plus DTT) at a concentration of 2 nM for different time periods. Then, the culture medium was discarded. The cells were collected and washed three times with 1 × Dulbecco's phosphate-buffered saline (DPBS; Life Technologies) and resuspended in 1 ml of DPBS. The uptake level was then expressed as the UV–Vis absorbance and the circular dichroism signal.

Isothermal titration calorimetry (ITC) studies

The chiral nanocrystals (100 μM) were suspended in DPBS and injected into the CD97 or EMR1 (10 μM) with 1.96 μl per injection (injection interval 300 s; 25 injections in total). The thermodynamic effects were measured using a Nano ITC Low Volume (TA Instrument, USA). The stirring rate was 300 r.p.m. during the measurements. Data were analysed using the original NanoAnalyze software.

In vitro activation and cytokine secretion

Mouse BMMs and BMDCs were seeded into 6-well plates (10^6 cells per well) and cultured with 2 μg ml^{-1} MPL, 20 μg ml^{-1} OVA and L-nanoparticles, L-P^{+10} nanoparticle, L-P^{+15} nanoparticles, L-P^{+20} nanoparticles, L-P^{+25} nanoparticles, L-P$^+$ nanoparticles, prism, D-nanoparticles, D-P^{-10} nanoparticles, D-P^{-15} nanoparticles, D-P^{-20} nanoparticles, D-P^{-25} nanoparticles, D-P$^-$ nanoparticles, PBS, PEG, L-CYP, D-CYP, nanoparticles, NP-D-CYP, NP-L-CYP, NS-L-CYP, NS-D-CYP, L-P$^+$ nanoparticles plus DTT, or D-P$^+$ nanoparticles plus DTT (2 nM each), for 12 h. Afterwards, the supernatant was collected and the production of IL-12 (BD, 555256) and IL-1β (JKBio Shanghai, JLC3580) was estimated using an enzyme-linked immunosorbent assay (ELISA) kit. Cells were harvested and stained using anti-CD86 monoclonal antibody (GL1), anti-CD40 monoclonal antibody (1C10), anti-CD80 monoclonal antibody (16-10A1), anti-OVA257-264 (SIINFEKL) peptide bound to H-2Kb monoclonal antibody (25-D1.16), anti-MHC class II (I-A/I-E) monoclonal antibody (M5/114), or anti-TNF-α (TN3-19.12). Flow-cytometry data were analysed using FlowJo10.3 and GraphPad prism software.

Western blotting analysis

For the western blotting analysis, mouse BMDCs (1.0×10^6) cultured in cell medium were collected, and their proteins were extracted with RIPA lysis buffer IV (Beyotime). Protein lysates were separated using sodium dodecyl sulfate (SDS)–polyacrylamide gel electrophoresis (PAGE) and transferred onto polyvinylidene difluoride (PVDF) membranes; blots were processed according to the manufacturer's protocol (Sangon Biotech). The PVDF membranes were incubated with a primary antibody (diluted 1:1,000) directed against clathrin, dynamin NLRP3, IL-1β, pro-caspase-1, caspase-1, pro-IL-1β, gasdermin D, cleaved gasdermin D, pro-IL-18 or IL-18 and then with a horseradish-peroxidase (HRP)-conjugated secondary antibody (1:500 dilution). β-Actin was used as a loading control.

Human BMDCs (1.0×10^6) cultured in the specified cell medium were collected and their proteins were extracted with RIPA lysis buffer IV (Beyotime). Protein lysates were separated with SDS–PAGE and transferred onto polyvinylidene difluoride (PVDF) membranes; blots were processed according to the manufacturer's protocol (western blot analysis kit from Sangon Biotech). The PVDF membranes were incubated with a primary antibody (diluted 1:1,000) directed against CD97 or EMR1, and then with a HRP-conjugated secondary antibody (1:500 dilution). β-Actin was used as a loading control.

Confocal microscopy imaging

Intracellular transport of nanoparticles was observed by confocal microscopy. The cells were seeded in a 35 mm Petri dish and cultured for 24 h to achieve a density of 10^4 cells per plate. The cells were then incubated with nanomaterials (L-P$^+$ nanoparticles, D-P$^-$ nanoparticles, L-P$^+$ nanoparticles plus DTT, D-P$^-$ nanoparticles plus DTT, and Cy3-PEG-L-P$^+$ nanoparticles, 2 nM) in culture medium for different times. The culture medium was discarded; the cells were washed three times with DPBS, fixed with 4% paraformaldehyde for 10 min, stained with DAPI (Beyotime, C1005) and observed by laser scanning confocal microscopy (Leica TCS SP8). The grey values of the white dots were then analysed using LAS AF Lite software. To estimate the ability to recruit dynamin, the cells stained with Cy5-labelled anti-CD97 antibody, Cy5-labelled anti-EMR1 dynamin antibody (Cell Signaling Technology, catalogue number 2342S), or anti-clathrin antibody (Cell Signaling Technology, 4796S), and then stained with Goat anti-Rabbit IgG (H+L) secondary antibody (Thermofisher, 84541).

We confirmed that the immune response to chiral nanoparticles is mediated by CD97 and EMR1 by using fluorescence resonance energy transfer (FRET) microscopy during uptake of Cy3-labelled L-P$^+$ nanoparticles via Cy5-labelled receptors. Excitation at 540 nm in the absorption band of Cy3, where the Cy5 label serves as a FRET acceptor in this pair, emitted only when nanoparticles and CD97 or EMR1 formed a complex. The localization of L-P$^+$ nanoparticles with respect to other parts of the cell was monitored by Cy3 emission. After incubation with mouse BMDCs, the intensity of red emission from Cy5–CD97 in the cell membrane gradually increased (Fig. 4f and Supplementary Fig. 23), indicating that L-P$^+$ nanoparticles bound to the extracellular domain of the receptor. As the incubation time increased, so FRET emission from CD97 increased, confirming the formation of nanoparticle–CD97 complexes. The nanoparticles then entered the cells and the Cy5 intensity on the cell membrane gradually decreased, while the intracellular Cy3 signal (green colour) gradually increased, indicating endocytosis. For D-P$^-$ nanoparticles, FRET emission was much weaker (Supplementary Fig. 23). Similar processes were observed for Cy5–EMR1 (Fig. 4g and Supplementary Fig. 23), indicating that both nanoparticle–CD97 and nanoparticle–EMR1 complexes form, which mediate the endocytosis of nanoparticles by mouse BMDCs. TPL imaging also showed that L-P$^+$ nanoparticles became co-localized with dynamin and clathrin, proving that these two proteins facilitate the endocytosis of nanoparticles into mouse BMDCs (Fig. 4h and Supplementary Fig. 23).

A series of control flow-cytometry experiments showed that only minimal amounts of nanoparticles were found inside mouse BMDCs after blocking CD97, EMR1, dynamin or clathrin (Fig. 4e and Supplementary Fig. 23), confirming that L-P$^+$ nanoparticles entered the cells by binding to CD97 or EMR1, with downstream recruitment of dynamin and clathrin. The stronger binding of L-P$^+$ nanoparticles to CD97 and EMR1 causes the higher cellular uptake of L-P$^+$ nanoparticles compared with D-P$^-$ nanoparticles (Figs. 3a, 4c, d and Supplementary Fig. 23).

We also tested nanoparticle uptake by human BMDCs[33] that carry CD97 receptors (Extended Data Fig. 1a, b and Supplementary Fig. 24). FRET, TPL and flow-cytometry data reproduced the uptake and localization patterns observed for murine cells, indicating the commonality of nanoparticle endocytosis mediated by AGPCR receptors. The intensity of CD97–Cy5 emission with L-P$^+$ nanoparticles was also much higher than with D-P$^-$ nanoparticle (Extended Data Fig. 1b and Supplementary Fig. 24).

Inflammasome activation

Mouse BMDCs collected from wild-type or NLRP3$^{-/-}$ C57BL/6 mice were incubated with 2 μg ml^{-1} MPL, 20 μg ml^{-1} OVA and 2 nM L-nanoparticles, L-P^{+10} nanoparticles, L-P^{+15} nanoparticles, L-P^{+20} nanoparticles, L-P^{+25} nanoparticles, L-P$^+$ nanoparticles, prism, D-nanoparticles, D-P^{-10} nanoparticles, D-P^{-15} nanoparticles, D-P^{-20} nanoparticles, D-P^{-25} nanoparticles, D-P$^-$ nanoparticles, PBS, L-CYP, D-CYP, nanoparticles, NP-D-CYP, NP-L-CYP, NS-L-CYP or NS-D-CYP (2 nM), for 12 h. Concentrations of IL-1β, IL-18, pro-IL-1β, pro-IL-18, caspase-1, lactate dehydrogenase, IL-2 and IL-6 in the culture medium were measured with an ELISA kit. Cells were treated with an anti-NLRP3 antibody and Alexa Fluor 488-conjugated goat anti-rabbit IgG secondary antibody, and NLRP3 expression was measured by confocal imaging, flow cytometry and RT–PCR. Expression of the immune genes *CXCL2*, *NEK7*, *caspase-1*, *IL-18*, *IL-1β*, *TNF-α*, *IL-6*, *IL-2*, *CXCL1* and *IL-12p40* was measured by RT–PCR (see Supplementary Table 3). To explore the signalling pathway downstream of inflammasome activation by chiral nanoparticles, we pretreated mouse BMDCs with MCC950 (10 μM), chlorpromazine (50 μM), cytochalasin D (2 μM), *N*-acetyl-L-cysteine (NAC, 5 mM), amiodarone (40 μM), KCl (130 mM), dynasore (80 μM), nocodazole

(10 μM) or CA-074-Me (5 μM) for 2 h, and then cultured them with L-P^+ nanoparticles (2 nM) or D-P^+ nanoparticles (2 nM) for 12 h.

Wild-type or NLRP3$^{-/-}$ C57BL/6 mice were subcutaneously immunized with different chiral nanoparticles (2 mg), MPL (10 μg) and OVA (50 μg). After 36 h, the dLNs were collected. Expression of NLRP3 in mouse BMDCs was analysed by flow cytometry.

In vivo immune responses

Wild-type or NLRP3$^{-/-}$ C57BL/6 mice were subcutaneously immunized with prism (2 mg) plus MPL (10 μg) plus OVA (50 μg); L-nanoparticles (2 mg) plus MPL (10 μg) plus OVA (50 μg); L-P^{+10} nanoparticles (2 mg) plus MPL (10 μg) plus OVA (50 μg); L-P^{+15} nanoparticles (2 mg) plus MPL (10 μg) plus OVA (50 μg); L-P^{+20} nanoparticles (2 mg) plus MPL (10 μg) plus OVA (50 μg); L-P^{+25} nanoparticles (2 mg) plus MPL (10 μg) plus OVA (50 μg); L-P^+ nanoparticles (2 mg) plus MPL (10 μg) plus OVA (50 μg); D-nanoparticles (2 mg) plus MPL (10 μg) plus OVA (50 μg); D-P^{-10} nanoparticles (2 mg) plus MPL (10 μg) plus OVA (50 μg); D-P^{-15} nanoparticles (2 mg) plus MPL (10 μg) plus OVA (50 μg); D-P^{-20} nanoparticles (2 mg) plus MPL (10 μg) plus OVA (50 μg); D-P^{-25} nanoparticles (2 mg) plus MPL (10 μg) plus OVA (50 μg); D-P^- nanoparticles (2 mg) plus MPL (10 μg) plus OVA (50 μg); PBS plus MPL (10 μg) plus OVA (50 μg); PEG (10 mg) pls MPL (10 μg) plus OVA (50 μg); L-CYP (10 μg) plus MPL (10 μg) plus OVA (50 μg); D-CYP (10 μg) plus MPL (10 μg) plus OVA (50 μg); nanoparticles (2 mg) plus MPL (10 μg) plus OVA (50 μg); L-P^+ nanoparticles with DTT (2 mg) plus MPL (10 μg) plus OVA (50 μg); D-P^- nanoparticles with DTT (2 mg) plus MPL (10 μg) plus OVA (50 μg); NS-L-CYP (2 mg) plus MPL (10 μg) plus OVA (50 μg); NS-D-CYP (2 mg) plus MPL (10 μg) plus OVA (50 μg); NP-L-CYP (2 mg) plus MPL (10 μg) plus OVA (50 μg); or NP-D-CYP (2 mg) plus MPL (10 μg) plus OVA (50 μg).

To evaluate the maturation of mouse BMDCs in vivo, mice were euthanized 36 h after immunization, and the inguinal lymph nodes collected to prepare single-cell suspensions. Cells were stained using the following antibodies: fluorescein isothiocyanate (FITC)-labelled anti-CD11c monoclonal antibody (N418); peridinin chlorophyll protein (PerCP)–eFluor710 anti-CD40 monoclonal antibody (1C10); phycoerythrin (PE)-labelled anti-CD80 monoclonal antibody (16-10A1); allophycocyanin (APC)-labelled anti-CD86 monoclonal antibody (GL1); OVA257-264 (SIINFEKL) peptide bound to H-2Kb monoclonal antibody (25-D1.16); and MHC class II (I-A/I-E) monoclonal antibody (M5/114) (eBioscience, Thermo Fisher Scientific).

To analyse immune responses, mice were euthanized at 0 and 14 days, and splenocytes were harvested 7 days after the last immunization. Splenocytes were stimulated overnight with OVA, and cell activation cocktail with brefeldin A (Biolegend, 423304) was added to the cell culture in the final 4 h. Splenocytes were stained with FITC-labelled anti-CD3e monoclonal antibody (145-2C11), APC-labelled anti-CD8a monoclonal antibody (53-6.7), PE–Cy7-labelled rat anti-mouse TNF-α (MP6-XT22), and PerCP–cyanine5.5 anti-IFN-γ monoclonal antibody (XMG1.2). To evaluate immune memory, splenocytes were co-stained with FITC-labelled anti-CD3e monoclonal antibody (145-2C11), APC-labelled anti-CD8a monoclonal antibody (53-6.7), PE-labelled anti-CD44 monoclonal antibody (IM7), and PE–Cyanine7-labelled anti-CD62L monoclonal antibody (MEL-14). All of the antibodies were obtained from eBioscience, Thermo Fisher, unless otherwise indicated. Dilution of antibodies for flow-cytometry staining was performed according to the manufacturer's protocols.

Influenza vaccination

C57BL/6 mice were immunized at 0 and 14 days with the indicated formulations including H9N2 influenza vaccine (10^8 ELD_{50}/0.1 ml, 60 μl); MPL (10 μg); L-P^+ nanoparticles (2 mg) plus H9N2 plus MPL; D-P^- nanoparticles (2 mg) plus H9N2 plus MPL; alum (Thermo Fisher Scientific, 77161) plus H9N2 plus MPL; L-P^+ nanoparticles with DTT (2 mg) plus H9N2 plus MPL; D-P^- nanoparticles with DTT (2 mg) plus H9N2 plus MPL; NS-L-CYP (2 mg) plus H9N2 plus MPL; NS-D-CYP (2 mg) plus H9N2 plus MPL. Seven days after immunization, mice were euthanized and splenocytes were harvested and stimulated with the influenza virus for 12 h. Cell activation cocktail with brefeldin A (Biolegend, 423304) was added to the cell culture in the final 4 h. Splenocytes were stained with FITC-labelled anti-CD3e monoclonal antibody (145-2C11), APC-labelled anti-CD8a monoclonal antibody (53-6.7), PE–Cy7-labelled rat anti-mouse TNF-α (MP6-XT22), PerCP–Cyanine5.5-labelled anti-IFN-γ monoclonal antibody (XMG1.2), and PE-labelled anti-IL-4 monoclonal antibody (11B11). Antibodies were diluted for flow cytometry according to the manufacturer's protocols. Immunized mice were challenged with H9N2 influenza virus 14 days after the last immunization. Twenty-one days after challenge, mice were euthanized, and lungs were harvested for haematoxylin-and-eosin staining.

Antibody titre test

C57BL/6 mice were immunized with OVA (50 μg) or H9N2 influenza vaccine (10^8 ELD_{50}/0.1 ml, 60 μl) with the indicated adjuvants, including MPL, alum (Thermo Fisher Scientific, 77161) plus MPL, D-P^- nanoparticles plus MPL, or L-P^+ nanoparticles plus MPL, three times (days 1, 14 and 56). OVA- or H9N2-specific serum IgG titres were collected for 91 days and measured by ELISA according to the manufacturer's protocol (JingMei Biotechnology).

Reproducibility

A representative of at least three independent experiments is shown in Fig. 3b–j, 4c–e and Extended Data Figs. 1a, 2.

Reporting summary

Further information on research design is available in the Nature Research Reporting Summary linked to this paper.

Data availability

Source data for Figs. 3, 4 and Extended Data Figs. 1, 2 are provided with this paper. The data supporting the findings of this study are available within the paper and its Supplementary Information files. Source data are provided with this paper.

46. Chen, L. et al. High-yield seedless synthesis of triangular gold nanoplates through oxidative etching. *Nano Lett.* **14**, 7201–7206 (2014).
47. Johnson, P. B. & Christy, R. W. Optical constants of the noble metals. *Phys. Rev. B* **6**, 4370–4379 (1972).

Acknowledgements This work was financially supported by the National Natural Science Foundation of China (21925402, 32071400, 21977038, 92156003), Natural Science Foundation of Jiangsu Province (BK20212014), and Young Elite Scientist Sponsorship Program by China Association for Science and Technology (CAST) (2019QNRC001). N.A.K thanks the US National Science Foundation (NSF) (grants 1463474 and 1566460) for support. A.F.M. thanks the Brazilian Ministério da Educação (MEC)/Tutorial Education Programme (PET) for a fellowship and Conselho Nacional de Desenvolvimento Científico e Tecnológico (CNPq) for a research fellowship (311353/2019-3). We thank the Brazilian funding agencies Coordenação de Aperfeiçoamento de Pessoal de Nível Superio (CAPES), CNPq, and Fundação de Amparo à Pesquisa do Estado de São Paulo (FAPESP) (processes 2012/15147-4 and 2013/07296-2) for financial support; and the high-performance computer (HPC) resources provided by the SDumont supercomputer at the National Laboratory for Scientific Computing (Laboratório Nacional de Computação Científica (LNCC)/Ministério da Ciência, Tecnologia e Inovações (MCTI), Brazil; http://sdumont.lncc.br) and by the Cloud@UFSCar.

Author contributions H.K., N.A.K. and C.X. conceived the project and planned the experiments. L.X., X. Wang, C.H., S.L. and X. Wu fabricated the chiral nanoparticles. L.X., W.W., M.S., A.Q., M.L. and X.G. carried out immunological experiments. X. Wang and X.G. measured the affinity constant between chiral nanoparticles and receptors. L.X., M.S., A.Q. and M.L. carried out the inflammasome experiments. W.J.C. carried out electromagnetic modelling and simulation. J.-Y.K. calculated the chirality measures. F.M.C., W.R.G., A.L.B. and A.F.D. carried out electrodynamics calculations. L.X., H.K., N.A.K. and C.X. conceptualized the work, wrote the manuscript, and compiled figures, with discussion of results and feedback on the manuscript from all authors.

Competing interests The authors declare no competing interests.

Additional information
Supplementary information The online version contains supplementary material available at https://doi.org/10.1038/s41586-021-04243-2.

Correspondence and requests for materials should be addressed to Hua Kuang, Nicholas A. Kotov or Chuanlai Xu.

Peer review information *Nature* thanks Jacques Neefjes, Luke O'Neill and the other, anonymous, reviewer(s) for their contribution to the peer review of this work. Peer review reports are available.

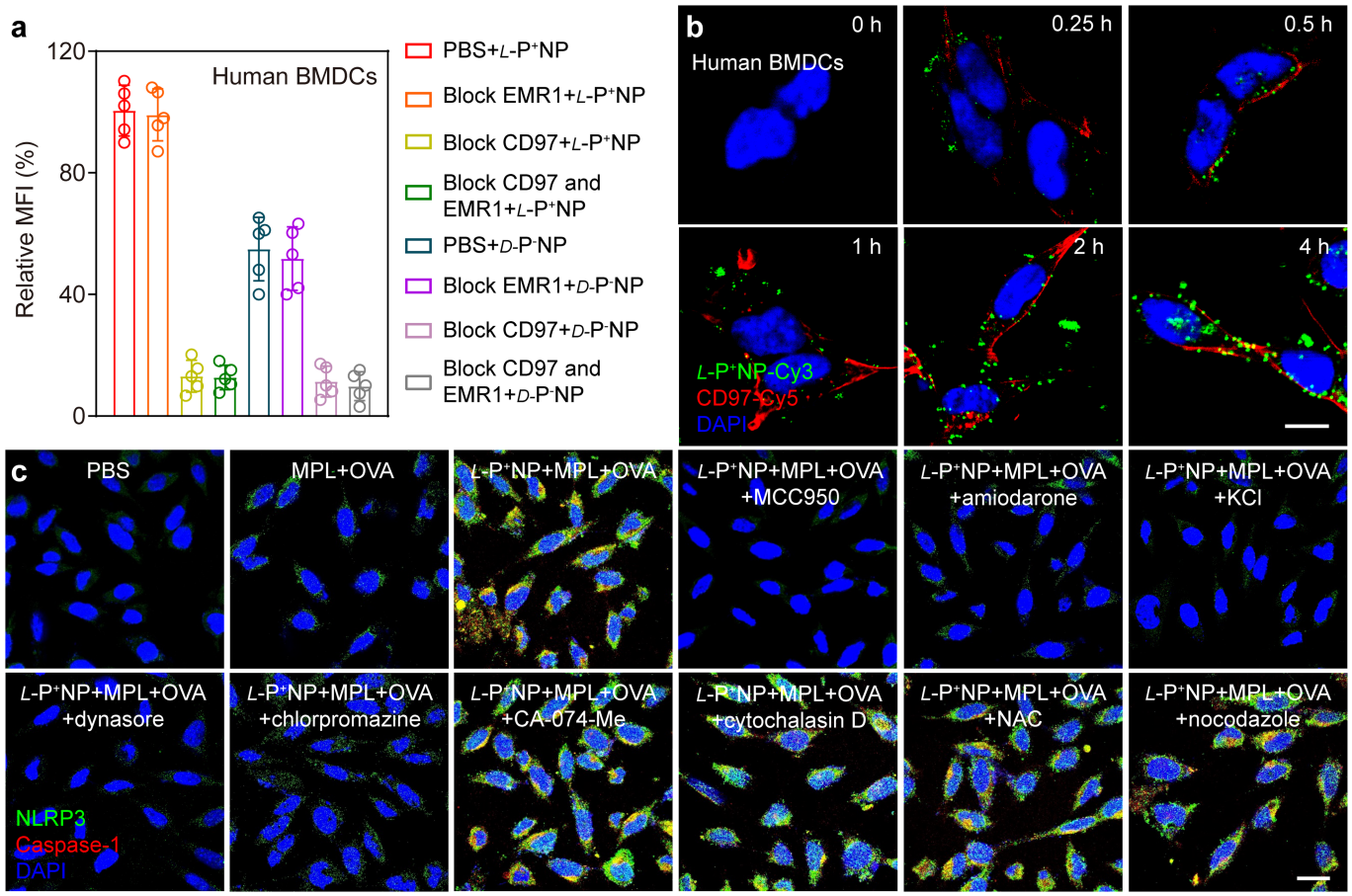

Extended Data Fig. 1 | Chiral nanoparticles are taken up by human BMDCs and activate inflammasomes. a, Flow-cytometry data for human BMDCs after being treated with PBS, anti-EMR1 antibody (30 μg ml^{-1}, blocking EMR1), anti-CD97 antibody (20 μg ml^{-1}, blocking CD97), or both anti-EMR1 antibody (30 μg ml^{-1}) and anti-CD97 antibody (20 μg ml^{-1}) (blocking both CD97 and EMR1) and then incubated with L-P$^+$ NP(2 nM) or D-P$^-$ NP (2 nM) for 8 h. **b**, Confocal imaging of human BMDCs incubated with 2 μg ml^{-1} MPL, 20 μg ml^{-1} OVA and 2 nM L-P$^+$ NP with various incubation times up to 4 h. Blue, DAPI; red, CD97–Cy5; green: L-P$^+$ NP–Cy3. Scale bar, 10 μm. **c**, Confocal imaging of NLRP3 inflammasome activation in mouse BMDCs after incubation with PBS, MPL plus OVA, L-P$^+$ NP + MPL + OVA, L-P$^+$ NP + MPL + OVA + MCC950 (NLRP3 inhibitor), L-P$^+$ NP + MPL + OVA + amiodarone (K$^+$-channel inhibitor), L-P$^+$ NP + MPL + OVA + KCl (K$^+$-efflux inhibitor), L-P$^+$ NP + MPL + OVA + dynasore (dynamin inhibitor), L-P$^+$ NP + MPL + OVA + chlorpromazine (clathrin inhibitor), L-P$^+$ NP + MPL + OVA + CA-074-Me (cathepsin B inhibitor), L-P$^+$ NP + MPL + OVA + cytochalasin D (phagocytosis inhibitor), L-P$^+$ NP + MPL + OVA + NAC (inhibitor of reactive oxygen species, ROS) and L-P$^+$ NP + MPL + OVA + nocodazole (microtubule inhibitor) for 12 h. Blue, DAPI; red, caspase-1; green, NLRP3. Scale bar, 20 μm. Data are mean ± s.d. ($n = 5$). *$P < 0.05$, **$P < 0.01$, ***$P < 0.001$, analysed by Student's t-test.

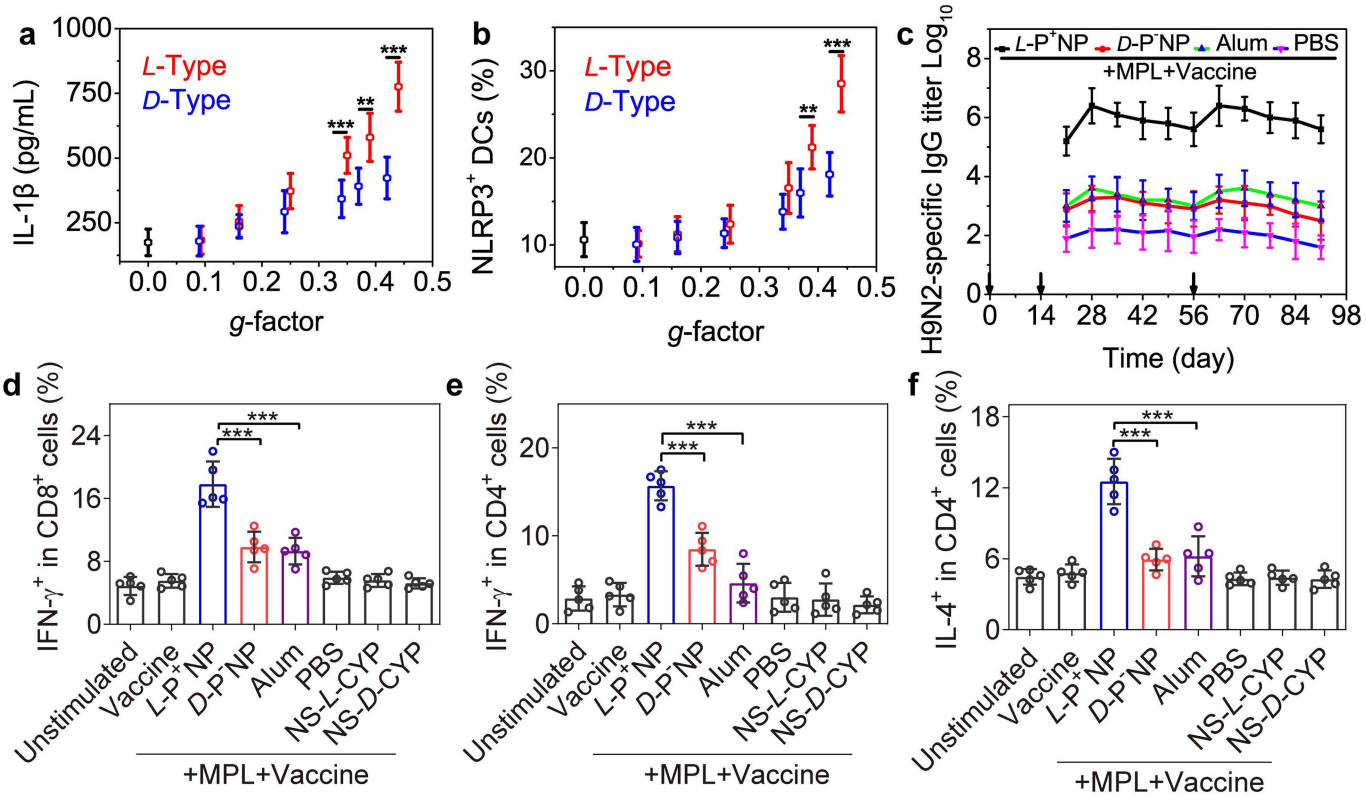

Extended Data Fig. 2 | Chirality-dependent efficiency of vaccination in mice. a, IL-1β concentration in the culture medium of mouse BMDCs after incubation with chiral nanoparticles of different *g*-factors, measured by ELISA. **b**, Expression of NLRP3 in wild-type mice after treatment with chiral nanoparticles of different *g*-factors, detected by flow cytometry. **c**–**f**, Influenza vaccination. C57BL/6 mice ($n = 5$) were immunized with H9N2 influenza vaccine and the indicated adjuvants, including MPL, alum + MPL, D-P$^-$ NP + MPL, L-P$^+$ NP + MPL, NS-D-CYP + MPL, or NS-L-CYP + MPL. **c**, The serum of the mice was collected to measure vaccine-specific antibody titres. **d**–**f**, IFN-γ-secreting CD8$^+$ T cells (**d**), IFN-γ-secreting CD4$^+$ T cells (**e**) and IL-4-secreting CD4$^+$ T cells (**f**) in the spleen were measured by flow cytometry 7 days after immunization. Data are means ± s.d. ($n = 5$). $^*P < 0.05$, $^{**}P < 0.01$, $^{***}P < 0.001$, analysed by Student's *t*-test.

nature portfolio

Corresponding author(s): Hua Kuang, Nicholas A. Kotov, Chuanlai Xu

Last updated by author(s): Oct 10, 2021

Reporting Summary

Nature Portfolio wishes to improve the reproducibility of the work that we publish. This form provides structure for consistency and transparency in reporting. For further information on Nature Portfolio policies, see our Editorial Policies and the Editorial Policy Checklist.

Statistics

For all statistical analyses, confirm that the following items are present in the figure legend, table legend, main text, or Methods section.

n/a	Confirmed	
☐	☒	The exact sample size (*n*) for each experimental group/condition, given as a discrete number and unit of measurement
☐	☒	A statement on whether measurements were taken from distinct samples or whether the same sample was measured repeatedly
☐	☒	The statistical test(s) used AND whether they are one- or two-sided *Only common tests should be described solely by name; describe more complex techniques in the Methods section.*
☐	☒	A description of all covariates tested
☐	☒	A description of any assumptions or corrections, such as tests of normality and adjustment for multiple comparisons
☐	☒	A full description of the statistical parameters including central tendency (e.g. means) or other basic estimates (e.g. regression coefficient) AND variation (e.g. standard deviation) or associated estimates of uncertainty (e.g. confidence intervals)
☐	☒	For null hypothesis testing, the test statistic (e.g. *F*, *t*, *r*) with confidence intervals, effect sizes, degrees of freedom and *P* value noted *Give P values as exact values whenever suitable.*
☒	☐	For Bayesian analysis, information on the choice of priors and Markov chain Monte Carlo settings
☒	☐	For hierarchical and complex designs, identification of the appropriate level for tests and full reporting of outcomes
☒	☐	Estimates of effect sizes (e.g. Cohen's *d*, Pearson's *r*), indicating how they were calculated

Our web collection on statistics for biologists contains articles on many of the points above.

Software and code

Policy information about availability of computer code

Data collection	Gatan Microscopy Suite Software, Leica LAS AF Lite, Living Image, Imaging Lab, Chirascan, ITC run, Lumerical FDTD Solutions, 3D graphic, MATLAB, VESTA 3, xtb, tda.
Data analysis	OriginPro 8.5, Microsoft excel, GraphPad prism, NanoAnalyze, CytExpert

For manuscripts utilizing custom algorithms or software that are central to the research but not yet described in published literature, software must be made available to editors and reviewers. We strongly encourage code deposition in a community repository (e.g. GitHub). See the Nature Portfolio guidelines for submitting code & software for further information.

Data

Policy information about availability of data

All manuscripts must include a data availability statement. This statement should provide the following information, where applicable:

- Accession codes, unique identifiers, or web links for publicly available datasets
- A description of any restrictions on data availability
- For clinical datasets or third party data, please ensure that the statement adheres to our policy

Provide your data availability statement here.

Field-specific reporting

Please select the one below that is the best fit for your research. If you are not sure, read the appropriate sections before making your selection.

☒ Life sciences ☐ Behavioural & social sciences ☐ Ecological, evolutionary & environmental sciences

For a reference copy of the document with all sections, see nature.com/documents/nr-reporting-summary-flat.pdf

Life sciences study design

All studies must disclose on these points even when the disclosure is negative.

Sample size	All the experiments were performed in three replicated or more. Sample sizes for experiments were estimated based on previous experience with a similar setup that showed significance. For cell experiments, 1000000 cells were collected for each sample. Statistics were derived when at least 3 independent samples were analyzed. Experiments involved mice were divided into 56 groups, while 5 animals being analyzed for each group and each group was performed three replicated.
Data exclusions	No data was excluded from the analyzes.
Replication	For each experiment and condition, at least three independent technical replicates were performed with similar results. All observations reported in the manuscript were reproducible.
Randomization	The mice applied in this experiment were randomly selecting and divided into different groups, each group contain five mice.
Blinding	The investigators were blinded to group allocation during data collection and/or analysis. All samples were analyzed using the reported approach without prior knowledge of their levels.

Behavioural & social sciences study design

All studies must disclose on these points even when the disclosure is negative.

Study description	*Briefly describe the study type including whether data are quantitative, qualitative, or mixed-methods (e.g. qualitative cross-sectional, quantitative experimental, mixed-methods case study).*
Research sample	*State the research sample (e.g. Harvard university undergraduates, villagers in rural India) and provide relevant demographic information (e.g. age, sex) and indicate whether the sample is representative. Provide a rationale for the study sample chosen. For studies involving existing datasets, please describe the dataset and source.*
Sampling strategy	*Describe the sampling procedure (e.g. random, snowball, stratified, convenience). Describe the statistical methods that were used to predetermine sample size OR if no sample-size calculation was performed, describe how sample sizes were chosen and provide a rationale for why these sample sizes are sufficient. For qualitative data, please indicate whether data saturation was considered, and what criteria were used to decide that no further sampling was needed.*
Data collection	*Provide details about the data collection procedure, including the instruments or devices used to record the data (e.g. pen and paper, computer, eye tracker, video or audio equipment) whether anyone was present besides the participant(s) and the researcher, and whether the researcher was blind to experimental condition and/or the study hypothesis during data collection.*
Timing	*Indicate the start and stop dates of data collection. If there is a gap between collection periods, state the dates for each sample cohort.*
Data exclusions	*If no data were excluded from the analyses, state so OR if data were excluded, provide the exact number of exclusions and the rationale behind them, indicating whether exclusion criteria were pre-established.*
Non-participation	*State how many participants dropped out/declined participation and the reason(s) given OR provide response rate OR state that no participants dropped out/declined participation.*
Randomization	*If participants were not allocated into experimental groups, state so OR describe how participants were allocated to groups, and if allocation was not random, describe how covariates were controlled.*

Ecological, evolutionary & environmental sciences study design

All studies must disclose on these points even when the disclosure is negative.

Study description	*Briefly describe the study. For quantitative data include treatment factors and interactions, design structure (e.g. factorial, nested, hierarchical), nature and number of experimental units and replicates.*

Research sample	*Describe the research sample (e.g. a group of tagged Passer domesticus, all Stenocereus thurberi within Organ Pipe Cactus National Monument), and provide a rationale for the sample choice. When relevant, describe the organism taxa, source, sex, age range and any manipulations. State what population the sample is meant to represent when applicable. For studies involving existing datasets, describe the data and its source.*
Sampling strategy	*Note the sampling procedure. Describe the statistical methods that were used to predetermine sample size OR if no sample-size calculation was performed, describe how sample sizes were chosen and provide a rationale for why these sample sizes are sufficient.*
Data collection	*Describe the data collection procedure, including who recorded the data and how.*
Timing and spatial scale	*Indicate the start and stop dates of data collection, noting the frequency and periodicity of sampling and providing a rationale for these choices. If there is a gap between collection periods, state the dates for each sample cohort. Specify the spatial scale from which the data are taken*
Data exclusions	*If no data were excluded from the analyses, state so OR if data were excluded, describe the exclusions and the rationale behind them, indicating whether exclusion criteria were pre-established.*
Reproducibility	*Describe the measures taken to verify the reproducibility of experimental findings. For each experiment, note whether any attempts to repeat the experiment failed OR state that all attempts to repeat the experiment were successful.*
Randomization	*Describe how samples/organisms/participants were allocated into groups. If allocation was not random, describe how covariates were controlled. If this is not relevant to your study, explain why.*
Blinding	*Describe the extent of blinding used during data acquisition and analysis. If blinding was not possible, describe why OR explain why blinding was not relevant to your study.*

Did the study involve field work? ☐ Yes ☐ No

Field work, collection and transport

Field conditions	*Describe the study conditions for field work, providing relevant parameters (e.g. temperature, rainfall).*
Location	*State the location of the sampling or experiment, providing relevant parameters (e.g. latitude and longitude, elevation, water depth).*
Access & import/export	*Describe the efforts you have made to access habitats and to collect and import/export your samples in a responsible manner and in compliance with local, national and international laws, noting any permits that were obtained (give the name of the issuing authority, the date of issue, and any identifying information).*
Disturbance	*Describe any disturbance caused by the study and how it was minimized.*

Reporting for specific materials, systems and methods

We require information from authors about some types of materials, experimental systems and methods used in many studies. Here, indicate whether each material, system or method listed is relevant to your study. If you are not sure if a list item applies to your research, read the appropriate section before selecting a response.

Materials & experimental systems

n/a	Involved in the study
☐	☒ Antibodies
☐	☒ Eukaryotic cell lines
☐	☐ Palaeontology and archaeology
☐	☒ Animals and other organisms
☐	☐ Human research participants
☐	☐ Clinical data
☐	☐ Dual use research of concern

Methods

n/a	Involved in the study
☐	☐ ChIP-seq
☐	☒ Flow cytometry
☐	☐ MRI-based neuroimaging

Antibodies

Antibodies used	FITC CD11c Monoclonal Antibody (ThermoFisher, 11-0114-85, N418), PerCP/Cyanine 5.5 Anti-mouse CD40 Antibody (Biolegend, 124623, 3/23), PE CD80 Monoclonal Antibody (ThermoFisher, 12-0801-81, 16-10A1), APC CD86 Monoclonal Antibody (ThermoFisher, 17-0862-82, GL1), FITC CD3e Monoclonal Antibody (ThermoFisher, 11-0031-82, 145-2C11), APC CD8a Monoclonal Antibody (ThermoFisher, 17-0081-82, 53-6.7), PE-Cy7 Rat Anti-mouse TNF (ThermoFisher, 25-7321-82, MP6-XT22), PerCP-Cyanine 5.5 IFN-γ Monoclonal Antibody (BD Pharmingen, 557649, XMG1.2), PE Anti-Mouse IL-4 Antibody (Biolegend, 504103, 11B11), PE CD44 Monoclonal Antibody (ThermoFisher, 12-0441-82, IM7), PE-Cyanine 7 CD62L Monoclonal Antibody (ThermoFisher, 25-0612-82, MEL-14), Horseradish Peroxidase-conjugated Anti-Mouse IgG (Thermo Fisher Scientific, 62-6520), IL-12 (BD, 555256), EEA1 Anti-mouse Monoclonal Antibody (Santa Cruz Biotechnology, sc-137130), LAMP1 Anti-mouse Monoclonal Antibody (Santa Cruz Biotechnology, sc-20011), Dynamin 2 Anti-rabbit Polyclonal Antibody (Abcam, ab3457), Clathrin Heavy Chain Anti-mouse Monoclonal

Antibody (ThermoFisher, MA1-065), Anti-CD97 Mouse Monoclonal Antibody (Sino Biological, 11280-MM07), Anti-CD97 Mouse Monoclonal Antibody (Santa Cruz Biotechnology, sc-166852), Anti-EMR1 Mouse Monoclonal Antibody (Santa Cruz Biotechnology, sc-365340, D-11), Anti-TLR4 Rabbit polyclonal Antibody (Abcam, ab13556), Anti-NLRP3 Rabbit Antibody (Invitrogen, PA5-79740), Caspase-1 Anti-mouse IgG (Santa Cruz Biotechnology, sc-56036), Anti-β-actin Mouse Monoclonal Antibody (Santa Cruz Biotechnology, sc-47778), Anti-IL-18 Rabbit polyclonal Antibody (Abcam, ab71495), Anti-IL-1 beta Rabbit Polyclonal Antibody (Sino Biological, 50101-T48),Anti-IL1β Rabbit Polyclonal Antibody (solarbio, K009661P), IL-18 (E8P5O) Rabbit mAb (Cell Signaling Technology, 57058S), Cleaved Caspase-1 (Asp296) (E2G2I) Rabbit mAb (Cell Signaling Technology, 89332), Anti-GSDMD Rabbit Polyclonal Antibody (solarbio, K009328P), Cleaved Gasdermin D (Asp276) Antibody (Cell Signaling Technology, 50928)

Validation

FITC CD11c Monoclonal Antibody (Species Reactivity: Human, Mouse; Application: Flow, ICC, IF, IHC, IV), PerCP/Cyanine 5.5 Anti-mouse CD40 Antibody (Species Reactivity: Mouse; Application: Flow), PE CD80 Monoclonal Antibody (Species Reactivity: Pig, Mouse, Dog; Application: Flow, ICC, IF, IHC, IV), APC CD86 monoclonal Antibody (Species Reactivity: Mouse; Application: Flow), FITC CD3e Monoclonal Antibody (Species Reactivity: Mouse; Application: Flow, ICC, IF, IHC), APC CD8a Monoclonal Antibody (Species Reactivity: Mouse; Application: Flow), PE-Cy7 Rat Anti-mouse TNF (Species Reactivity: Mouse; Application: Flow), PerCP-Cyanine5.5 IFN-γ Monoclonal Antibody (Species Reactivity: Mouse; Application: Flow), PE anti-mouse IL-4 antibody (Species Reactivity: Mouse; Application: Flow), PE CD44 Monoclonal Antibody (Species Reactivity: Mouse; Application: Flow), PE-Cyanine 7 CD62L Monoclonal Antibody (Species Reactivity: Mouse; Application: Flow), anti-EMR1 (Species Reactivity: Mouse; Application: ELISA, IP, IF, WB), IL-12 (Species Reactivity: Mouse; Application: ELISA), HRP-conjugated Anti-mouse IgG (Species Reactivity: Mouse; Application: ELISA, IHC, WB, ICC, IHC), EEA1 Anti-mouse Monoclonal Antibody (Species Reactivity: Mouse, Rat, Human, Monkey; Application: WB, IP, IF, IHC, ELISA), LAMP1 Anti-mouse Monoclonal Antibody (Species Reactivity: Mouse, Rat, Human; Application: WB, IP, IF, FCM, IHC, ELISA), Dynamin 2 Anti-rabbit Polyclonal Antibody (Species Reactivity: Mouse, Rat, Human, Non-human primates; Application: ICC, WB, IHC-P), Clathrin Heavy Chain Anti-mouse Monoclonal Antibody (Species Reactivity: Bovine, Hamster, Human, Mouse, Non-human Primate, Rat; Application: IHC, WB, Flow, IP, IM, ICC), Anti-CD97 Mouse Monoclonal Antibody (Species Reactivity: Human; Application: ELISA, ICC/IF), Anti-CD97 Mouse Monoclonal Antibody (Species Reactivity: Mouse, Rat, Human; Application: IP, WB, IHC(P) , ELISA, IF, FCM), Anti-EMR1 Mouse Monoclonal Antibody (Species Reactivity: Human; Application: IP, WB, IHC(P) , ELISA, IF, FCM), Anti-TLR4 Rabbit Polyclonal Antibody (Species Reactivity: Mouse, Human, Recombinant Fragment; Application: WB, IHC-P, IHC-Fr, Flow Cyt), Anti-NLRP3 Rabbit Antibody (Species Reactivity: Mouse; Application: WB, IF, ICC, IHC(P), Flow Cyt), Caspase-1 Anti-mouse IgG (Species Reactivity: Mouse, Rat, Human; Application: WB, IP, IF, IHC), Anti-β-actin Mouse Monoclonal Antibody (Species Reactivity: Mouse, Rat, Human; Application: WB, IP, IF, IHC (P), ELISA), Anti-IL-18 Rabbit polyclonal Antibody (Species Reactivity: Mouse; Application: WB, IHC-P), Anti-IL-1 beta Rabbit Polyclonal Antibody (Species Reactivity: Mouse; Application: WB,ELISA), Anti-IL1β Rabbit Polyclonal Antibody (Species Reactivity: Human Mouse Rat Dog Horse Rabbit; Application: WB ELISA IHC-P IHC-F IF), IL-18 (E8P5O) Rabbit mAb (Species Reactivity: Mouse; Application: WB), Cleaved Caspase-1 (Asp296) (E2G2I) Rabbit mAb (Species Reactivity: Mouse; Application: WB,IP), Anti-GSDMD Rabbit Polyclonal Antibody (Species Reactivity: Human Mouse; Application: WB), Cleaved Gasdermin D (Asp276) Antibody (Species Reactivity: Mouse; Application: WB)

Eukaryotic cell lines

Policy information about cell lines

Cell line source(s)	Human bone-marrow-derived dendritic cells (BMDCs) were obtained from Procell Life Science&Technology Co.,Ltd.
Authentication	No cell lines authentication was performed.
Mycoplasma contamination	No testing for mycoplasma contamination was performed.
Commonly misidentified lines (See ICLAC register)	*Name any commonly misidentified cell lines used in the study and provide a rationale for their use.*

Palaeontology and Archaeology

Specimen provenance	No specimen were used.
Specimen deposition	No specimen were used.
Dating methods	No specimen were used.

☒ Tick this box to confirm that the raw and calibrated dates are available in the paper or in Supplementary Information.

Ethics oversight	No specimen were used.

Note that full information on the approval of the study protocol must also be provided in the manuscript.

Animals and other organisms

Policy information about studies involving animals; ARRIVE guidelines recommended for reporting animal research

Laboratory animals	Wild type C57BL/6 mice (8 weeks old) were obtained from Qinglong Mountain Animal Technology (Nanjing, China). NLRP3 knockout mice (NLRP3-/-) in C57BL/6 background were obtained from Cyagen Biosciences. After the study, the captive mice were killed by neck-breaking. Because it is the most common method of killing mice with minimal pain, in line with animal welfare.
Wild animals	No wild animals were used.
Field-collected samples	For in-vivo toxicity test, the liver and kidney were excised for hematoxylin and eosin staining. To evaluate the maturation of BMDCs

Field-collected samples	in-vivo, mice were euthanized and the inguinal lymph nodes collected to prepare single cell suspensions 36 h after immunization.To analyze immune responses, mice were euthanized and splenocytes were harvest 7 d post the last immunization. The immunized mice were challenged,with H9N2 influenza virus 14 days after immunization. 21 days after challenged, mice were euthanized and lungs were harvest for hematoxylin and eosin (H&E) staining.
Ethics oversight	All animal studies were performed according to institutional ethical guidelines and were approved by the Committee on Animal Welfare of Jiangnan University.

Note that full information on the approval of the study protocol must also be provided in the manuscript.

Human research participants

Policy information about studies involving human research participants

Population characteristics	No human research participants in this experiment.
Recruitment	No human research participants in this experiment.
Ethics oversight	No human research participants in this experiment.

Note that full information on the approval of the study protocol must also be provided in the manuscript.

Clinical data

Policy information about clinical studies

All manuscripts should comply with the ICMJE guidelines for publication of clinical research and a completed CONSORT checklist must be included with all submissions.

Clinical trial registration	No clinical studies in this experiment.
Study protocol	No clinical studies in this experiment.
Data collection	No clinical studies in this experiment.
Outcomes	No clinical studies in this experiment.

Dual use research of concern

Policy information about dual use research of concern

Hazards

Could the accidental, deliberate or reckless misuse of agents or technologies generated in the work, or the application of information presented in the manuscript, pose a threat to:

No	Yes	
☒	☐	Public health
☒	☐	National security
☒	☐	Crops and/or livestock
☒	☐	Ecosystems
☒	☐	Any other significant area

Experiments of concern

Does the work involve any of these experiments of concern:

No	Yes	
☒	☐	Demonstrate how to render a vaccine ineffective
☒	☐	Confer resistance to therapeutically useful antibiotics or antiviral agents
☒	☐	Enhance the virulence of a pathogen or render a nonpathogen virulent
☒	☐	Increase transmissibility of a pathogen
☒	☐	Alter the host range of a pathogen
☒	☐	Enable evasion of diagnostic/detection modalities
☒	☐	Enable the weaponization of a biological agent or toxin
☒	☐	Any other potentially harmful combination of experiments and agents

ChIP-seq

Data deposition

☐ Confirm that both raw and final processed data have been deposited in a public database such as GEO.

☐ Confirm that you have deposited or provided access to graph files (e.g. BED files) for the called peaks.

Data access links *May remain private before publication.*	No ChIP-seq were used in this experiment.
Files in database submission	No ChIP-seq were used in this experiment.
Genome browser session (e.g. UCSC)	No ChIP-seq were used in this experiment.

Methodology

Replicates	No ChIP-seq were used in this experiment.
Sequencing depth	No ChIP-seq were used in this experiment.
Antibodies	No ChIP-seq were used in this experiment.
Peak calling parameters	No ChIP-seq were used in this experiment.
Data quality	No ChIP-seq were used in this experiment.
Software	No ChIP-seq were used in this experiment.

Flow Cytometry

Plots

Confirm that:

☒ The axis labels state the marker and fluorochrome used (e.g. CD4-FITC).

☒ The axis scales are clearly visible. Include numbers along axes only for bottom left plot of group (a 'group' is an analysis of identical markers).

☒ All plots are contour plots with outliers or pseudocolor plots.

☒ A numerical value for number of cells or percentage (with statistics) is provided.

Methodology

Sample preparation	Provided in SI on page S11-12, S15-17
Instrument	Flow cytometry was performed on BD FACSAria II.
Software	Data were analyzed by FlowJo and GraphPad prism software.
Cell population abundance	Provided in SI on page S11-12, S15-17
Gating strategy	Provided in Figure share on Figshare Fig. 18, 20, 34

☐ Tick this box to confirm that a figure exemplifying the gating strategy is provided in the Supplementary Information.

Magnetic resonance imaging

Experimental design

Design type	No MRI imaging were used in this experiment.
Design specifications	No MRI imaging were used in this experiment.
Behavioral performance measures	No MRI imaging were used in this experiment.

Acquisition

Imaging type(s) — No MRI imaging were used in this experiment.

Field strength — No MRI imaging were used in this experiment.

Sequence & imaging parameters — No MRI imaging were used in this experiment.

Area of acquisition — No MRI imaging were used in this experiment.

Diffusion MRI ☐ Used ☒ Not used

Preprocessing

Preprocessing software — No MRI imaging were used in this experiment.

Normalization — No MRI imaging were used in this experiment.

Normalization template — No MRI imaging were used in this experiment.

Noise and artifact removal — No MRI imaging were used in this experiment.

Volume censoring — No MRI imaging were used in this experiment.

Statistical modeling & inference

Model type and settings — No MRI imaging were used in this experiment.

Effect(s) tested — No MRI imaging were used in this experiment.

Specify type of analysis: ☐ Whole brain ☐ ROI-based ☐ Both

Statistic type for inference (See Eklund et al. 2016) — No MRI imaging were used in this experiment.

Correction — *Describe the type of correction and how it is obtained for multiple comparisons (e.g. FWE, FDR, permutation or Monte Carlo).*

Models & analysis

n/a	Involved in the study
☐	☐ Functional and/or effective connectivity
☐	☐ Graph analysis
☐	☐ Multivariate modeling or predictive analysis

Functional and/or effective connectivity — No MRI imaging were used in this experiment.

Graph analysis — No MRI imaging were used in this experiment.

Multivariate modeling and predictive analysis — No MRI imaging were used in this experiment.